



Implementation and Application of Maximally Localized Wannier Functions within the (L)APW+lo Method

Abschlussarbeit zur Erlangung des akademischen Grades

Master of Science

M. Sc.

von

Sebastian Tillack

geboren am 27. Juni 1991 in Chemnitz

eingereicht am Institut für Physik
der Mathematisch-Naturwissenschaftlichen Fakultät
Humboldt-Universität zu Berlin

Betreuer: Dr. Andris Gulans
Prof. Dr. Dr. hc. Claudia Draxl

Erstgutachter: Prof. Dr. Dr. hc. Claudia Draxl

Zweitgutachter: Dr. Denis Usvyat

eingereicht am 12.01.2018

Der Gelehrte studiert die Natur nicht, weil das etwas Nützliches ist.

*Er studiert sie, weil er daran Freude hat,
und er hat Freude daran, weil sie so schön ist.*

*Wenn die Natur nicht so schön wäre,
so wäre es nicht der Mühe wert, sie kennen zu lernen,
und das Leben wäre nicht wert, gelebt zu werden.*

Henri Poincaré (1854-1912)

Contents

1. Introduction	1
2. Methodology and Theoretical Background	3
2.1. Density-functional theory	3
2.2. The tight-binding method	7
2.3. The (L)APW+lo method	8
2.4. Wannier functions	9
2.4.1. Definition and properties	10
2.4.2. Localization of Wannier functions	12
2.4.3. The spread-functional Ω	14
2.5. Construction of Wannier functions	16
2.5.1. The projection method	16
2.5.2. Optimized projection functions	17
2.5.3. Maximally localized Wannier functions	18
2.6. Wannier interpolation	20
2.6.1. Interpolation of the wavefunction	21
2.6.2. Interpolation of eigenenergies	22
3. Implementation	25
3.1. Workflow	25
3.2. Projection and choice of projection functions	27
3.3. Initial guess from simple projection	28
3.4. Initial guess from OPFs	30
3.5. Minimization of the spread Ω	32
3.5.1. Conjugate gradient and line-search	32
3.5.2. Calculation of the spread and its gradient	34
3.5.3. Convergence criteria	35
3.5.4. Starting point dependence and convergence	36
3.6. Interpolation	41
3.6.1. Choice of the lattice vector set \mathbf{R}	41
3.6.2. Interpolation of band-characters	42

4. Applications	45
4.1. Diamond-like structures	45
4.1.1. Band-structure interpolation	45
4.1.2. Chemical bonding analysis	47
4.2. Titanium dioxide	50
4.3. Hybrid organic–inorganic system	50
4.4. Metals	54
5. Conclusions and Outlook	57
References	VIII
List of Figures	IX
List of Abbreviations and Symbols	X
Appendices	XIII

1. Introduction

Ab-initio theory forms a pillar of materials science and allows for exploring and understanding all types of materials. A material's electronic and optical properties can be calculated from first principles using its quantum mechanical wavefunction. In the field of solid state physics, most calculations are carried out in the reciprocal-space, and the common way to do this is in terms of Bloch functions. This well established standard is used in codes that implement density-functional theory (DFT) and many-body perturbation theory. However, the complexity of the most interesting modern materials may come with immense computational costs, in particular when applying advanced theories. In order to make these state-of-the-art methods widely applicable to a multitude of elaborated materials, new concepts and algorithms need to be applied.

Wannier functions (WFs) form a mathematically equivalent representation to the Bloch formalism in which crystalline materials can be described [Wan37]. However, WFs are not uniquely defined, and some freedom remains in choosing them. This ambiguity can be overcome by calculating them such that they are maximally localized according to a given localization criterion. These maximally localized Wannier functions (MLWFs) make up an excellent tight-binding basis and, hence, a more effective but equally accurate framework for the calculation of electronic and optical properties compared to Bloch functions. Furthermore, MLWFs are much easier to interpret due to their localized nature in contrast to the fully delocalized Bloch waves.

The computation of many quantities (e.g. the electron density in metals) requires a dense sampling of the reciprocal-space. Typically, this becomes very expensive in the common Bloch representation. MLWFs, however, can be used to interpolate both wavefunctions and eigenenergies in reciprocal-space in the frame of a Slater–Koster interpolation [SK54] at low computational costs. A systematic way to obtain MLWFs from Bloch wavefunctions that have been calculated on a coarse set of points in reciprocal-space using e.g. DFT was provided by Marzari and Vanderbilt [MV97]. These MLWFs and the Bloch functions are related to each other by a set of unitary transformations and Fourier transforms.

The concept of Wannier interpolation offers access to plenty of various applications. The key quantity of interest in this work is the electronic band-structure which is obtained from interpolation built upon different levels of theory. We present the implementation of the Marzari–Vanderbilt approach within the full-potential linearized augmented plane wave

(FLAPW) + local orbital framework as implemented in the `exciting` code [Gul+14]. As an initial guess for the calculation of MLWFs we compute optimized projection functions (OPFs) [Mus+15] from local orbitals.

The obtained well and maximally localized WFs are applied to the interpolation of band-structures starting from simple Kohn–Sham (KS) eigenenergies obtained using local and semi-local exchange-correlation functionals, non-local hybrid functionals, and quasi-particle energies calculated within the G_0W_0 approximation. Band-structures are calculated for a variety of materials like simple diamond-like structures, metals and complex organic–inorganic hybrid systems. We demonstrate that eigenenergies can be interpolated up to an accuracy of a few meV and over wide energy ranges of about 100 eV.

2. Methodology and Theoretical Background

2.1. Density-functional theory

The major goal in solid-state physics and computational material science is the determination of properties and characteristics of many-body systems. In quantum mechanics, these can be derived from the many-body wavefunction Ψ which obeys the time-independent Schrödinger equation

$$\hat{H}\Psi(\mathbf{r}_i, \mathbf{R}_m) = E\Psi(\mathbf{r}_i, \mathbf{R}_m), \quad i = 1, \dots, N; \quad m = 1, \dots, M, \quad (2.1)$$

with the total energy E and the many-body Hamiltonian \hat{H}

$$\hat{H} = -\sum_{i=1}^N \frac{\nabla_i^2}{2} - \sum_{m=1}^M \frac{\nabla_m^2}{2M_m} + \frac{1}{2} \sum_{i \neq j} \frac{1}{|\mathbf{r}_i - \mathbf{r}_j|} - \sum_{i,m} \frac{Z_m}{|\mathbf{r}_i - \mathbf{R}_m|} + \frac{1}{2} \sum_{m \neq n} \frac{Z_m Z_n}{|\mathbf{R}_m - \mathbf{R}_n|}. \quad (2.2)$$

M_m , Z_m , and \mathbf{R}_m label the masses, charges, and positions of the nuclei and \mathbf{r}_i the positions of the electrons. Here and throughout this work, we use atomic units, i.e. $m_e = e = \hbar = 1$. In general, the wavefunction Ψ depends on $3(N + M)$ spatial coordinates where N and M are the total number of electrons and nuclei in the system, respectively. In a macroscopic sample, this number is in the order of Avogadro's constant ($\sim 10^{23}$). Thus, it is virtually impossible to explicitly calculate the full many-body wavefunction. In order to tackle this problem, several assumptions and simplifications are made.

First, the positions of the nuclei \mathbf{R}_m are considered to be fixed with respect to the electron coordinates. This is the so called Born–Oppenheimer approximation which is motivated by the much larger masses M_m of the nuclei compared to the electron mass and thereby with the larger inertia of the nuclei. From now on, we focus on the system of N interacting electrons in an external field caused by the nuclei. The electronic wavefunction $\Psi(\mathbf{r}_i)$ then is an eigenfunction of the electronic Hamiltonian

$$\hat{H} = -\sum_i \frac{\nabla_i^2}{2} + \frac{1}{2} \sum_{i \neq j} \frac{1}{|\mathbf{r}_i - \mathbf{r}_j|} - \sum_{i,m} \frac{Z_m}{|\mathbf{r}_i - \mathbf{R}_m|} = \hat{T} + \hat{U} + \hat{V}_{\text{ext}}. \quad (2.3)$$

The first term describes the kinetic energy \hat{T} of the electrons, the second term the electron–electron interaction \hat{U} , and the third term the external potential \hat{V}_{ext} . Note, that \hat{T} and \hat{U} are universal operators which are the same for each N -electron system

and just the potential \hat{V}_{ext} depends on the specific system. However, Ψ is still a function of $3N$ variables. The key idea to make this problem practical is the introduction of the electron density

$$n(\mathbf{r}) = N \int d\mathbf{r}_2 \dots d\mathbf{r}_N |\Psi(\mathbf{r}, \mathbf{r}_2, \dots, \mathbf{r}_N)|^2 \quad (2.4)$$

and two theorems proved by Hohenberg and Kohn [HK64]. The first theorem states that for a system of interacting electrons in an external potential $\hat{V}_{\text{ext}} = \sum_i v_{\text{ext}}(\mathbf{r}_i)$ the external potential is (up to a constant) a unique functional of the electron density, i.e. $\hat{V}_{\text{ext}} = \hat{V}_{\text{ext}}[n(\mathbf{r})]$. More explicit, $\hat{V}_{\text{ext}}[n(\mathbf{r})] = \int d\mathbf{r} v_{\text{ext}}(\mathbf{r})n(\mathbf{r})$. In particular, since \hat{T} and \hat{U} are universal, the wavefunction $\Psi = \Psi[n(\mathbf{r})]$ is a functional of the density as well. The second theorem states, that the density that minimizes the energy functional $\hat{E}[n] = \hat{T}[n] + \hat{U}[n] + \hat{V}_{\text{ext}}[n]$ uniquely defines the groundstate density and thus the groundstate wavefunction of an N -electron system in the external potential \hat{V}_{ext} . These fundamental findings reduce the solution of the above many-electron problem to finding the groundstate density $n_0(\mathbf{r})$ which is a function of only three variables. This is the major idea of density-functional theory (DFT). However, these theoretical considerations do not yet provide a practical tool to solve the many-electron problem. A solution was promoted by Kohn and Sham [KS65] who introduced a fictitious system of N non-interacting electrons in an effective external potential $v_{\text{KS}}(\mathbf{r})$ that gives rise to the same groundstate density as the interacting system. With that, the search for an N -particle wavefunction $\Psi(\mathbf{r}_i)$ can be divided in finding of N single-particle orbitals $\phi_n(\mathbf{r})$. Then, the total wavefunction is given by a single Slater determinant of these N orbitals. In order to find the $\phi_n(\mathbf{r})$, the yet unknown part of the energy functional is recast as

$$\hat{T}[n] + \hat{U}[n] = \hat{T}_0[n] + \frac{1}{2} \int d\mathbf{r} d\mathbf{r}' \frac{n(\mathbf{r})n(\mathbf{r}')}{|\mathbf{r} - \mathbf{r}'|} + \hat{E}_{\text{xc}}[n], \quad (2.5)$$

where the first term on the right-hand site describes the kinetic energy of non-interacting electrons. The second term describes the classical Coulomb interaction of the electrons (Hartree energy) and the third term, the so called exchange-correlation (xc) energy, includes all many-body effects that have not been accounted for. The groundstate density n_0 can be found by the application of the variational principle to the total energy func-

tional $\hat{\mathbf{E}}[n]$, and the introduction of a Lagrange multiplier ϵ ensures the conservation of the number of electrons. Eventually, this leads to

$$\delta\hat{\mathbf{E}}[n(\mathbf{r})] = \int d\mathbf{r} \left[\frac{\delta\hat{\mathbf{T}}_0[n(\mathbf{r})]}{\delta n(\mathbf{r})} + v_{\text{KS}}(\mathbf{r}) - \epsilon \right] \delta n(\mathbf{r}) = 0, \quad (2.6)$$

where

$$v_{\text{KS}}(\mathbf{r}) = v_{\text{H}}(\mathbf{r}) + v_{\text{ext}}(\mathbf{r}) + v_{\text{xc}}[n(\mathbf{r})] \quad (2.7)$$

denotes the Kohn–Sham (KS) potential, with the Hartree potential

$$v_{\text{H}}(\mathbf{r}) = \int d\mathbf{r}' \frac{n(\mathbf{r}')}{|\mathbf{r} - \mathbf{r}'|} \quad (2.8)$$

and the exchange-correlation potential

$$v_{\text{xc}}[n(\mathbf{r})] = \frac{\delta\hat{\mathbf{E}}_{\text{xc}}[n(\mathbf{r})]}{\delta n(\mathbf{r})}. \quad (2.9)$$

Note that (2.6) is equivalent to a system of non-interacting electrons in the presence of an external potential v_{KS} . Thus, the groundstate density can be obtained by solving a set of N single-particle Schrödinger equations known as KS equations

$$\left[-\frac{\nabla^2}{2} + v_{\text{KS}}(\mathbf{r}) \right] \phi_n(\mathbf{r}) = \epsilon_n \phi_n(\mathbf{r}) \quad (2.10)$$

for a set of single-particle wavefunctions ϕ_n (KS orbitals) from which the density is constructed as

$$n(\mathbf{r}) = \sum_{n=1}^N |\phi_n(\mathbf{r})|^2. \quad (2.11)$$

The subscript n labels the quantum number(s) that are necessary to describe the concrete system under consideration. Since v_{KS} itself depends on the density (and thus the orbitals), these equations have to be solved self-consistently.

All many-body effects are covered by the exchange-correlation potential v_{xc} which is universal but unknown. Over the time, numerous approximations of this quantity have been made. A potential in the local-density approximation (LDA) is local, i.e., $v_{\text{xc}}[n(\mathbf{r})]$ solely depends on $n(\mathbf{r})$ at one single point. The semi local generalized gradient approximation (GGA) also involves gradient of the density. Other potentials are non-local, i.e., they

usually depend on integrals over the density. Typically, these generalized KS-potentials partially overcome the well-known problem of under estimating band-gaps within pure KS-DFT by (partially) curing the self-interaction error present in (semi) local DFT. One example of non-local potentials that has been used within this work is the hybrid PBE0 potential [AB99]. Here, the xc-energy is expressed as

$$E_{\text{xc}}^{\text{PBE0}} = \frac{1}{4}E_{\text{x}}^{\text{HF}} + \frac{3}{4}E_{\text{x}}^{\text{PBE}} + E_{\text{c}}^{\text{PBE}} , \quad (2.12)$$

where $E_{\text{xc}}^{\text{PBE}}$ is the xc-energy from the GGA PBE functional [PBE96]. E_{x}^{HF} is the non-local Hartree–Fock exchange energy

$$E_{\text{x}}^{\text{HF}} = -\frac{1}{2} \sum_{m,n} \int \int d\mathbf{r}_1 d\mathbf{r}_2 \frac{\overline{\phi_m(\mathbf{r}_1)} \overline{\phi_n(\mathbf{r}_1)} \phi_m(\mathbf{r}_2) \phi_n(\mathbf{r}_2)}{|\mathbf{r}_1 - \mathbf{r}_2|} . \quad (2.13)$$

In solid-state physics, DFT is usually used to compute electronic properties of periodic crystals. The regular pattern of the nuclei in a crystal implies periodicity of the external potential $V_{\text{ext}}(\mathbf{r} + \mathbf{R}) = V_{\text{ext}}(\mathbf{r})$, where \mathbf{R} describes a lattice vector in real-space. According to Bloch’s theorem, the wavefunction of an electron in such a periodic potential takes the form $\Psi_{\mathbf{k}}(\mathbf{r}) = e^{i\mathbf{k}\cdot\mathbf{r}} u_{\mathbf{k}}(\mathbf{r})$ with a cell-periodic function $u_{\mathbf{k}}(\mathbf{r} + \mathbf{R}) = u_{\mathbf{k}}(\mathbf{r})$. For each reciprocal lattice vector \mathbf{G} , $\Psi_{\mathbf{k}+\mathbf{G}}$ is an equally valid wavefunction, thus \mathbf{k} is restricted to the first Brillouin zone (BZ) which is the Wigner–Seitz cell of the reciprocal lattice. For an infinite system, \mathbf{k} is continuous. In practice, however, one uses Born–von Kármán periodic boundary conditions, i.e., the infinite system is mimicked by $N_1 \times N_2 \times N_3$ repeating unit cells of the crystal. This also restricts the crystal momentum \mathbf{k} to a discrete $N_1 \times N_2 \times N_3$ grid in the BZ. Hence, the wavevector \mathbf{k} and the band-index n are the natural quantum numbers in periodic systems. Accordingly, we will refer to the single-particle wavefunctions in Eq. (2.10) as $\Psi_{n,\mathbf{k}}$ instead of ϕ_n in the following.

Another method that goes beyond DFT is many-body perturbation theory. Within this work, we use quasi-particle energies obtained within the so-called one-shot GW (also referred to as G_0W_0) method. Here, the quasi-particle energies $\epsilon_n^{\text{QP},\mathbf{k}}$ are obtained by the application of a correction term to the KS eigenvalues $\epsilon_n^{\mathbf{k}}$

$$\epsilon_n^{\text{QP},\mathbf{k}} = \epsilon_n^{\mathbf{k}} + \int \int d\mathbf{r}_1 d\mathbf{r}_2 \overline{\Psi_{n,\mathbf{k}}(\mathbf{r}_1)} \left[\text{Re}\{\Sigma(\mathbf{r}_1, \mathbf{r}_2; \epsilon_n^{\text{QP},\mathbf{k}})\} - V_{\text{xc}}(\mathbf{r}_1) \delta(\mathbf{r}_1 - \mathbf{r}_2) \right] \Psi_{n,\mathbf{k}}(\mathbf{r}_2) . \quad (2.14)$$

Here, $\Sigma = iG_0W_0$ is the self-energy which is approximated by the Green's function G_0 and the screened Coulomb potential W_0 of the non-interacting KS system. For a more detailed description of this method we refer to the literature (e.g. Ref. [AG98]).

2.2. The tight-binding method

The tight-binding method is one way to solve the many-electron problem as an approximate approach to find the single-electron crystal wavefunctions from strongly localized atomic orbitals. The periodic crystal potential $v(\mathbf{r})$ induced by basis atoms at sites \mathbf{R}_α is decomposed in single contributions $v_\alpha^{\text{at}}(\mathbf{r})$ of isolated atoms and the difference $\Delta v(\mathbf{r})$ to the actual crystal potential.

$$v(\mathbf{r}) = \sum_{\mathbf{R}} \sum_{\alpha} v_\alpha^{\text{at}}(\mathbf{r} - \mathbf{R}_\alpha - \mathbf{R}) + \Delta v(\mathbf{r}) , \quad (2.15)$$

where \mathbf{R} runs over all unit-cells of the crystal. Let's assume that $\chi_{\alpha j}^{\text{at}}(\mathbf{r})$ is an eigenfunction of the atomic single-particle Hamiltonian $\hat{\mathbf{h}}_\alpha^{\text{at}} = -\frac{\nabla^2}{2} + v_\alpha^{\text{at}}(\mathbf{r})$ with eigenenergy $\varepsilon_{\alpha j}$. Then, a Bloch wave $\phi_{m,\mathbf{k}}(\mathbf{r})$ can be constructed out of these atomic orbitals

$$\phi_{m,\mathbf{k}}(\mathbf{r}) = \frac{1}{\sqrt{N}} \sum_{\mathbf{R}} e^{i\mathbf{k}\cdot\mathbf{R}} \sum_{\alpha} e^{i\mathbf{k}\cdot\mathbf{R}_\alpha} \chi_{\alpha j}^{\text{at}}(\mathbf{r} - \mathbf{R}_\alpha - \mathbf{R}) , \quad (2.16)$$

where N is the total number of atomic states per unit-cell, and the band-index m labels the j -th atomic orbital at site \mathbf{R}_α . The actual single-electron crystal wavefunction $\Psi_{n,\mathbf{k}}(\mathbf{r})$ is then constructed as a linear combination of these Bloch waves

$$\Psi_{n,\mathbf{k}}(\mathbf{r}) = \sum_{m=1}^N C_{mn}^{\mathbf{k}} \phi_{m,\mathbf{k}}(\mathbf{r}) . \quad (2.17)$$

The coefficients $C_{mn}^{\mathbf{k}}$ and the eigenenergies $\varepsilon_n^{\mathbf{k}}$ are then found by solving the secular equation $\sum_m C_{mn}^{\mathbf{k}} (\hat{\mathbf{h}} - \varepsilon_n^{\mathbf{k}}) \phi_{m,\mathbf{k}}(\mathbf{r}) = 0$ with the full single-particle crystal Hamiltonian $\hat{\mathbf{h}}$.

This approach is valid only if the overlap between the atomic orbitals $\chi_{\alpha j}^{\text{at}}$ for adjacent atoms is sufficiently small, i.e., the electrons are tightly bound to the nucleus at \mathbf{R}_α . Thus, the accuracy of tight-binding calculations for electrons higher in energy, such as valence or conduction electrons, is often limited. Hence, the usage of this method is usually restricted to the description of core electrons and approximative to valence electrons. However, there are some notable advantages as well. First, the tight-binding approach

requires only a minimal basis while more accurate methods use much larger basis sets. Second, the resulting orbitals are easy to interpret due to their atomic nature, e.g. in terms of chemical bonding or symmetry. And third, once the atomic solutions $\chi_{\alpha j}^{\text{at}}$ are known, it is rather simple to obtain solutions for arbitrary \mathbf{k} -points since the \mathbf{k} -dependent Bloch waves are constructed from them using a simple Fourier-sum (2.16). Hence, this approach can be used as an interpolation scheme starting from the solutions of a more accurate method as suggested by Slater and Koster [SK54].

2.3. The (L)APW+lo method

Within this work, augmented plane waves (APWs) together with local orbitals are used as basis functions for solving the KS equations. This method provides a very accurate gold standard to solve Eq. (2.10) numerically. Within this framework, the unit cell is partitioned in an interstitial region (I) and muffin-tin spheres (MTs) α . The MTs are non-overlapping spheres of radius R_α centered at all atomic sites \mathbf{R}_α . I is the space in between these spheres where the basis functions are pure plane waves. These are augmented inside the MTs with a spherical harmonic expansion. Thus, the APW basis functions read

$$\phi_{\mathbf{G}+\mathbf{k}}(\mathbf{r}) = \begin{cases} \sum_{lm} A_{lm, \mathbf{G}+\mathbf{k}}^\alpha u_l^\alpha(r_\alpha) Y_{lm}(\hat{\mathbf{r}}_\alpha) & \mathbf{r} \in \text{MT}_\alpha \\ \frac{1}{\Omega_c} e^{i(\mathbf{G}+\mathbf{k}) \cdot \mathbf{r}} & \mathbf{r} \in I. \end{cases} \quad (2.18)$$

Here, Ω_c denotes the unit-cell volume and $\mathbf{r}_\alpha = \mathbf{r} - \mathbf{R}_\alpha$. \mathbf{G} is a reciprocal lattice vector restricted by the condition $|\mathbf{G} + \mathbf{k}| < G_{\text{max}}$ where G_{max} is a parameter that defines the energy cut-off of the used plane waves. The matching coefficients $A_{lm, \mathbf{G}+\mathbf{k}}^\alpha$ are chosen such that $\phi_{\mathbf{G}+\mathbf{k}}$ is continuous at the MT boundaries. The radial functions u_l^α are solutions of the radial Schrödinger equation

$$\left[\frac{1}{2} \frac{d^2}{dr^2} + \frac{l(l+1)}{2r^2} + v_0^\alpha(r) - \epsilon_n^{\mathbf{k}} \right] (r u_l^\alpha(r)) = 0, \quad (2.19)$$

where $v_0^\alpha(r)$ is the spherically-symmetric averaged potential inside the MT α , and $\epsilon_n^{\mathbf{k}}$ are the KS eigenvalues (Eq. (2.10)). The latter fact reveals the difficulty that the basis functions themselves depend on the KS eigenvalues $\epsilon_n^{\mathbf{k}}$. To solve this issue, one can either use a fixed energy parameter or the problem can be linearized by adding energy derivatives

in the spirit of a Taylor expansion. Adding the first derivative, the latter leads to linearized APWs where the MT part is expressed as

$$\phi_{\mathbf{G}+\mathbf{k}}(\mathbf{r}) = \sum_{lm} \left[A_{lm,\mathbf{G}+\mathbf{k}}^\alpha u_l^\alpha(r_\alpha; \epsilon_{l\alpha}) + B_{lm,\mathbf{G}+\mathbf{k}}^\alpha \dot{u}_l^\alpha(r_\alpha; \epsilon_{l\alpha}) \right] Y_{lm}(\hat{\mathbf{r}}_\alpha), \quad (2.20)$$

where \dot{u}_l^α denotes the first energy derivative of u_l^α , and $\epsilon_{l\alpha}$ is a fixed energy parameter. More generally, in higher orders of ϵ , this reads

$$\phi_{\mathbf{G}+\mathbf{k}}(\mathbf{r}) = \sum_{lm} \sum_o A_{lm,o,\mathbf{G}+\mathbf{k}}^\alpha u_{l,o}^\alpha(r_\alpha; \epsilon_{l\alpha}) Y_{lm}(\hat{\mathbf{r}}_\alpha), \quad (2.21)$$

with the o -th energy derivative $u_{l,o}^\alpha$. In the following we refer to this generalized augmentation scheme as (L)APW. Another way to linearize the problem can be performed by adding another type of basis functions to the APWs, which are called local orbitals. These are non-zero just within a single MT α_L and defined by

$$\phi_L(\mathbf{r}) = \left[\sum_o a_o^L u_{l_L,o}^{\alpha_L}(r_{\alpha_L}) \right] Y_{l_L m_L}(\hat{\mathbf{r}}_{\alpha_L}) = f_{l_L}^L(\mathbf{r}_\alpha) Y_{l_L m_L}(\hat{\mathbf{r}}_{\alpha_L}). \quad (2.22)$$

The coefficients a_o^L are chosen such that ϕ_L is normalized and zero at the MT boundary. With these additional functions, the basis set is highly flexible and can be adapted to a specific problem, offering highly accurate solutions of the KS equations which in the (L)APW+lo basis eventually read

$$\Psi_{n,\mathbf{k}}(\mathbf{r}) = \sum_{\mathbf{G}+\mathbf{k}} C_{n,\mathbf{G}}^{\mathbf{k}} \phi_{\mathbf{G}+\mathbf{k}}(\mathbf{r}) + \sum_L C_{n,L}^{\mathbf{k}} \phi_L(\mathbf{r}). \quad (2.23)$$

Solving Eq. (2.10) means finding the corresponding expansion coefficients $C_n^{\mathbf{k}}$.

2.4. Wannier functions

In 1937, the Swiss physicist Gregory H. Wannier discussed the Hamiltonian of an insulating crystal in terms of localized atomic-like wavefunctions instead of cell-periodic Bloch waves [Wan37]. He presented a method to construct such orbitals out of Bloch waves. These functions, commonly known as Wannier functions (WFs), have the major advantage over atomic functions to be orthogonal, and WFs form a representation of an electronic state that is perfectly equivalent to the Bloch representation. Hence, they form an or-

thonormal basis of the subspace spanned by the states within an energy band. Therefore, WFs can be used within a tight-binding approach with the advantage of – unlike purely atomic functions – being exact.

2.4.1. Definition and properties

Following Ref. [Wan37], the mathematical definition of a WF $w_{n,\mathbf{R}}(\mathbf{r})$ corresponding to an energy band n in the Bloch framework is given by

$$w_{n,\mathbf{R}}(\mathbf{r}) = \frac{V}{(2\pi)^3} \int_{\text{BZ}} e^{-i\mathbf{k}\cdot\mathbf{R}} \Psi_{n,\mathbf{k}}(\mathbf{r}) d\mathbf{k} , \quad (2.24)$$

where \mathbf{R} is a real-space lattice vector. In the bra-ket notation, a WF is represented by $|n\mathbf{R}\rangle$ such that $\langle \mathbf{r} | n\mathbf{R} \rangle = w_{n,\mathbf{R}}(\mathbf{r})$. Accordingly, the Bloch function $\Psi_{n,\mathbf{k}}(\mathbf{r})$ represents the state $|n\mathbf{k}\rangle$. The functions defined by Eq. (2.24) inherit the orthonormality of the Bloch states:

$$\begin{aligned} \langle n\mathbf{R} | n'\mathbf{R}' \rangle_{\mathbb{R}^3} &= \frac{V^2}{(2\pi)^6} \int_{\text{BZ}} d\mathbf{k} e^{i\mathbf{k}\cdot\mathbf{R}} \int_{\text{BZ}} d\mathbf{k}' e^{-i\mathbf{k}'\cdot\mathbf{R}'} \langle n\mathbf{k} | n'\mathbf{k}' \rangle_{\mathbb{R}^3} \\ &= \frac{V}{(2\pi)^3} \int_{\text{BZ}} d\mathbf{k} e^{i\mathbf{k}\cdot\mathbf{R}} \int_{\text{BZ}} d\mathbf{k}' e^{-i\mathbf{k}'\cdot\mathbf{R}'} \delta_{nn'} \delta(\mathbf{k} - \mathbf{k}') \\ &= \frac{V}{(2\pi)^3} \int_{\text{BZ}} d\mathbf{k} e^{i\mathbf{k}\cdot(\mathbf{R}-\mathbf{R}')} \delta_{nn'} \\ &= \delta_{nn'} \delta_{\mathbf{R}\mathbf{R}'} . \end{aligned} \quad (2.25)$$

In line two we made use of the normalization convention of our Bloch states. They are normalized within one unit cell Ω_c , that means $\langle n\mathbf{k} | n'\mathbf{k}' \rangle_{\Omega_c} = \delta_{nn'} \delta(\mathbf{k} - \mathbf{k}')$. Integration over the entire volume \mathbb{R}^3 then cancels one of the prefactors. The integral in the third line together with the remaining prefactor gives the Fourier representation of the delta distribution. For the sake of clarity and to avoid ambiguity, throughout this work we

name the integration domain \mathcal{D} whenever the bra-ket-notation is used with a superscript $\langle \cdot | \cdot \rangle^{\mathcal{D}}$. The Bloch periodicity of $\Psi_{n,\mathbf{k}}(\mathbf{r})$ is reflected in the WFs as well

$$\begin{aligned} w_{n,\mathbf{R}}(\mathbf{r} + \mathbf{R}') &= \frac{V}{(2\pi)^3} \int_{\text{BZ}} e^{-i\mathbf{k}\cdot\mathbf{R}} \Psi_{n,\mathbf{k}}(\mathbf{r} + \mathbf{R}') d\mathbf{k} \\ &= \frac{V}{(2\pi)^3} \int_{\text{BZ}} e^{-i\mathbf{k}\cdot(\mathbf{R}-\mathbf{R}')} \Psi_{n,\mathbf{k}}(\mathbf{r}) d\mathbf{k} \\ &= w_{n,\mathbf{R}-\mathbf{R}'}(\mathbf{r}) . \end{aligned} \quad (2.26)$$

We see that, for a given band index n , a WF depends only on the difference $\mathbf{r} - \mathbf{R}$, and two WFs with equal band indices, but different lattice vectors \mathbf{R} and \mathbf{R}' , are identical images that are shifted with respect to each other by the difference lattice vector $\mathbf{R} - \mathbf{R}'$. It means that each WF can be expressed in terms of the corresponding WF in the unit cell located at $\mathbf{R} = 0$ (referred to as the *home* unit cell),

$$w_{n,\mathbf{R}}(\mathbf{r}) = w_{n,0}(\mathbf{r} - \mathbf{R}) . \quad (2.27)$$

Using Born–von–Kármán boundary conditions (and hence a discrete \mathbf{k} -mesh), the BZ integral in Eq. (2.24) transforms into a discrete sum

$$w_{n,\mathbf{R}}(\mathbf{r}) = \frac{1}{N_{\mathbf{k}}} \sum_{\mathbf{k}} e^{-i\mathbf{k}\cdot\mathbf{R}} \Psi_{n,\mathbf{k}}(\mathbf{r}) d\mathbf{k} , \quad (2.28)$$

where $N_{\mathbf{k}}$ is the number of BZ mesh points. Then, the orthonormality relation in Eq. (2.25) holds for a supercell (SC) conjugate to the \mathbf{k} -point mesh $\langle n\mathbf{R} | n'\mathbf{R}' \rangle^{\text{SC}} = \delta_{nn'} \delta_{\mathbf{R}\mathbf{R}'}$ and the WFs become SC-periodic. Inverting equation (2.28) gives us an expression for the Bloch waves in terms of the WFs

$$\Psi_{n,\mathbf{k}}(\mathbf{r}) = \sum_{\mathbf{R}} e^{i\mathbf{k}\cdot\mathbf{R}} w_{n,\mathbf{R}}(\mathbf{r}) , \quad (2.29)$$

and the normalization convention for the Bloch states $\langle n\mathbf{k} | n'\mathbf{k}' \rangle^{\text{SC}} = N_{\mathbf{k}} \delta_{nn'} \delta_{\mathbf{k}\mathbf{k}'}$.

2.4.2. Localization of Wannier functions

The Bloch waves $\Psi_{n,\mathbf{k}}$ are uniquely defined only up to an arbitrary phase factor that creates an ambiguity in WFs. To illustrate this, we consider two Bloch functions $\Psi_{n,\mathbf{k}}$ and $\psi_{n,\mathbf{k}}$ that differ only in the phase, obeying the relation

$$\psi_{n,\mathbf{k}} = e^{i\varphi_n(\mathbf{k})} \Psi_{n,\mathbf{k}}, \quad (2.30)$$

where

$$\varphi_n(\mathbf{k} + \mathbf{G}) = \varphi_n(\mathbf{k}) + \mathbf{G} \cdot \Delta\mathbf{R}, \quad (2.31)$$

with \mathbf{G} and $\Delta\mathbf{R}$ being reciprocal- and real-space lattice vectors, respectively. $\Psi_{n,\mathbf{k}}$ and $\psi_{n,\mathbf{k}}$ are two entirely equivalent representations of the state $|n\mathbf{k}\rangle$ and neither of them is preferred over the other one according to the Schrödinger equation. WFs constructed using $\psi_{n,\mathbf{k}}$ read

$$w_{n,\mathbf{R}}(\mathbf{r}) = \frac{1}{N_{\mathbf{k}}} \sum_{\mathbf{k}} e^{i\mathbf{k}\cdot\mathbf{R}} \psi_{n,\mathbf{k}}(\mathbf{r}) = \frac{1}{N_{\mathbf{k}}} \sum_{\mathbf{k}} e^{i\mathbf{k}\cdot\mathbf{R}} e^{i\varphi_n(\mathbf{k})} \Psi_{n,\mathbf{k}}(\mathbf{r}), \quad (2.32)$$

and differ from those constructed from $\Psi_{n,\mathbf{k}}$ by both shape and position [Mar+12]. The latter corresponds to a shift by $\Delta\mathbf{R}$ in Eq. (2.31). Thus, the freedom of choice in $\varphi_n(\mathbf{k})$ leads to a pronounced ambiguity in WFs. In order to resolve the problem of ambiguity, we require a similarity with the tight-binding approach, i.e. we want to choose $\varphi_n(\mathbf{k})$ such that the resulting WFs are well localized. In other words, $\varphi_n(\mathbf{k})$ is chosen such that the transformed wavefunctions $\psi_{n,\mathbf{k}}$ are possibly smooth in \mathbf{k} . As a result, smoothness in reciprocal-space leads to localization in real-space what is an intrinsic property of the Fourier transform in Eq. (2.24). Up to now, we have just considered the single-band case, i.e. the index n represents a single and 'isolated' (i.e. separated in energy from all other bands throughout the BZ) band. However, Eq. (2.30) can be generalized to an isolated subspace of J bands. The states included in the selected subspace are mixed according to a set of unitary transformations $U^{\mathbf{k}}$ yielding a new set of J mixed states

$$\psi_{n,\mathbf{k}}(\mathbf{r}) = \sum_{m=1}^J U_{mn}^{\mathbf{k}} \Psi_{m,\mathbf{k}}(\mathbf{r}). \quad (2.33)$$

These Bloch functions form an equivalent representation of the subspace under consideration although they are no longer eigenstates of the Hamiltonian. Now, the WFs are constructed from these mixed states according to Eq. (2.28)

$$w_{n,\mathbf{R}}(\mathbf{r}) = \frac{1}{N_{\mathbf{k}}} \sum_{\mathbf{k}} e^{-i\mathbf{k}\cdot\mathbf{R}} \psi_{n,\mathbf{k}}(\mathbf{r}) \quad (2.34)$$

and become well localized assuming an appropriate choice of the unitary transformations $U^{\mathbf{k}}$. In the multi-band case, it is no longer meaningful to call n a band-index since the one-to-one mapping of the index n of the WF and the band-index of a specific eigenstate is lost due to the mixing in Eq. (2.33). Therefore, in the multi-band case, n is called a band-like index and we cannot associate a WF with one specific band. Instead, we associate a set of WFs with a set of eigenstates. The WFs constructed from the mixed states in Eq. (2.33) carry the same physical information of the subspace as the original Bloch waves $\Psi_{n,\mathbf{k}}$ do. So, they form an orthonormal basis of the considered subspace.

In order to quantify the term *localization*, we need to define a measure. There is a variety of them discussed in literature ([Nie72; ER63; PM89]) especially used for molecular systems where the selected subspace usually coincides with all the J occupied states. In applications to solid-state systems, Marzari and Vanderbilt [MV97] have adopted the Foster–Boys localization scheme [FB60]. The criterion used by them minimizes the quantity

$$\Omega = \sum_{n=1}^J \left[\langle n\mathbf{0} | \hat{\mathbf{r}}^2 | n\mathbf{0} \rangle^{\text{SC}} - \langle n\mathbf{0} | \hat{\mathbf{r}} | n\mathbf{0} \rangle^{\text{SC}2} \right], \quad (2.35)$$

which measures the quadratic spread of the position operator $\hat{\mathbf{r}}$ in the WFs in the home unit cell. This is the localization criterion we use in present work. In contrast to Eq. (2.35), Foster and Boys [FB60] carry out the integrals using molecular orbitals in the entire space \mathbb{R}^3 instead of orbitals in a crystal SC. Regardless of the used localization criterion, a WF $w_{n,\mathbf{0}}$ will be called to be localized when the overlap with its SC-periodic images is sufficiently small. This localization measure allows us to define maximally localized Wannier functions (MLWFs) which are the WFs that minimize Ω . The resulting WFs are unique just with respect to the chosen localization criterion. Another criterion may lead to a different set of MLWFs.

In practice, generating well-localized WFs is mathematically equivalent to the search of a set of unitary transformations $U^{\mathbf{k}}$ that yield a possibly small value for the spread $\Omega = \Omega[\{U^{\mathbf{k}}\}]$ which is a functional of these transformations.

2.4.3. The spread-functional Ω

In order to search for a set $U^{\mathbf{k}}$ systematically, one needs to establish how Ω depends on the transformation matrices. We sketch the derivation previously shown in Ref. [MV97]. First, the sum in Eq. (2.35) is split into three different contributions

$$\Omega_{\text{I}} = \sum_{n=1}^J \left[\langle n\mathbf{0} | \hat{\mathbf{r}}^2 | n\mathbf{0} \rangle^{\text{SC}} - \sum_{m=1}^J \sum_{\mathbf{R}} |\langle m\mathbf{R} | \hat{\mathbf{r}} | n\mathbf{0} \rangle^{\text{SC}}|^2 \right], \quad (2.36)$$

$$\Omega_{\text{D}} = \sum_{n=1}^J \sum_{\mathbf{R} \neq \mathbf{0}} |\langle n\mathbf{R} | \hat{\mathbf{r}} | n\mathbf{0} \rangle^{\text{SC}}|^2, \quad (2.37)$$

and

$$\Omega_{\text{OD}} = \sum_{m \neq n}^J \sum_{\mathbf{R}} |\langle m\mathbf{R} | \hat{\mathbf{r}} | n\mathbf{0} \rangle^{\text{SC}}|^2, \quad (2.38)$$

such that

$$\Omega = \Omega_{\text{I}} + \Omega_{\text{D}} + \Omega_{\text{OD}}. \quad (2.39)$$

Ω_{I} , Ω_{D} and Ω_{OD} are the independent, diagonal and off-diagonal part of the spread-functional, respectively. Ω_{I} is positive definite and independent of the choice of the unitary transformations $U^{\mathbf{k}}$ [MV97]. Marzari and Vanderbilt [MV97] derived an expression for Ω in the reciprocal-space representation using a relation for the matrix elements of the position operator in WFs as shown by Blount [Blo62]

$$\langle m\mathbf{R} | \hat{\mathbf{r}} | n\mathbf{0} \rangle^{\text{SC}} = i \frac{V}{(2\pi)^3} \int d\mathbf{k} e^{i\mathbf{k} \cdot \mathbf{R}} \langle m_{n,\mathbf{k}} | \nabla_{\mathbf{k}} | u_{n,\mathbf{k}} \rangle^{\Omega_{\text{c}}}, \quad (2.40)$$

where $u_{n,\mathbf{k}}(\mathbf{r}) = e^{-i\mathbf{k} \cdot \mathbf{r}} \psi_{n,\mathbf{k}}(\mathbf{r})$ is the cell-periodic part of the mixed Bloch waves in Eq. (2.33). Similarly, one obtains

$$\langle m\mathbf{R} | \hat{\mathbf{r}}^2 | n\mathbf{0} \rangle^{\text{SC}} = -\frac{V}{(2\pi)^3} \int d\mathbf{k} e^{i\mathbf{k} \cdot \mathbf{R}} \langle u_{m,\mathbf{k}} | \nabla_{\mathbf{k}}^2 | u_{n,\mathbf{k}} \rangle^{\Omega_{\text{c}}}. \quad (2.41)$$

In practical calculations, the BZ is sampled using a finite \mathbf{k} -mesh and $\nabla_{\mathbf{k}}$ is approximated by finite differences of a \mathbf{k} -point and its nearest neighbors. Then, following Ref. [MV97], Eqs. (2.36-2.38) transform into

$$\Omega_{\text{I}} = \frac{1}{N_{\mathbf{k}}} \sum_{\mathbf{k}, \mathbf{b}} w_{\mathbf{b}} \left(J - \sum_{m,n} |M_{mn}^{\mathbf{k}, \mathbf{b}}|^2 \right), \quad (2.42)$$

$$\Omega_D = \frac{1}{N_{\mathbf{k}}} \sum_{\mathbf{k}, \mathbf{b}} w_{\mathbf{b}} \sum_n \left(\text{Im}\{\ln M_{nn}^{\mathbf{k}, \mathbf{b}}\} + \mathbf{b} \cdot \langle \mathbf{r} \rangle_n \right)^2, \quad (2.43)$$

and

$$\Omega_{OD} = \frac{1}{N_{\mathbf{k}}} \sum_{\mathbf{k}, \mathbf{b}} w_{\mathbf{b}} \sum_{m \neq n} |M_{mn}^{\mathbf{k}, \mathbf{b}}|^2. \quad (2.44)$$

Here, \mathbf{b} is a vector connecting \mathbf{k} with one of its nearest neighbors and the sum over \mathbf{b} runs over all neighbors of \mathbf{k} taken into account in the finite difference representation of $\nabla_{\mathbf{k}}$. $w_{\mathbf{b}}$ denotes a corresponding geometric weight for the neighbors, which need to be chosen such that the condition

$$\sum_{\mathbf{b}} w_{\mathbf{b}} \mathbf{b} \mathbf{b}^T = \mathbb{1} \quad (2.45)$$

is satisfied. $\langle \mathbf{r} \rangle_n = \langle n\mathbf{0} | \hat{\mathbf{r}} | n\mathbf{0} \rangle^{\text{SC}}$ represents the center at which the WF $w_{n, \mathbf{0}}(\mathbf{r})$ is located. The matrices $M^{\mathbf{k}, \mathbf{b}}$ are defined as

$$M_{mn}^{\mathbf{k}, \mathbf{b}} = \langle u_{m, \mathbf{k}} | u_{n, \mathbf{k} + \mathbf{b}} \rangle^{\Omega_c} = \langle \psi_{m, \mathbf{k}} | e^{-i\mathbf{b} \cdot \mathbf{r}} | \psi_{n, \mathbf{k} + \mathbf{b}} \rangle^{\Omega_c}. \quad (2.46)$$

In terms of the original (unmixed) states $\Psi_{n, \mathbf{k}}$, this equation reads

$$\begin{aligned} M_{mn}^{\mathbf{k}, \mathbf{b}} &= \sum_{\mu, \nu} \overline{U_{\mu m}^{\mathbf{k}}} \langle \mu \mathbf{k} | e^{-i\mathbf{b} \cdot \mathbf{r}} | \nu \mathbf{k} + \mathbf{b} \rangle^{\Omega_c} U_{\nu n}^{\mathbf{k} + \mathbf{b}} \\ \Leftrightarrow M^{\mathbf{k}, \mathbf{b}} &= U^{\mathbf{k} \dagger} \mathcal{M}^{\mathbf{k}, \mathbf{b}} U^{\mathbf{k} + \mathbf{b}}, \end{aligned} \quad (2.47)$$

with

$$\mathcal{M}_{mn}^{\mathbf{k}, \mathbf{b}} = \langle m \mathbf{k} | e^{-i\mathbf{b} \cdot \mathbf{r}} | n \mathbf{k} + \mathbf{b} \rangle^{\Omega_c}. \quad (2.48)$$

These are the plane wave matrix elements of the original states. The total spread Ω then is calculated as

$$\Omega[\{U^{\mathbf{k}}\}] = \frac{1}{N_{\mathbf{k}}} \sum_{\mathbf{k}, \mathbf{b}} w_{\mathbf{b}} \sum_n \left[1 - |M_{nn}^{\mathbf{k}, \mathbf{b}}|^2 + \left(\text{Im}\{\ln M_{nn}^{\mathbf{k}, \mathbf{b}}\} + \mathbf{b} \cdot \langle \mathbf{r} \rangle_n \right)^2 \right], \quad (2.49)$$

and

$$\langle \mathbf{r} \rangle_n = -\frac{1}{N_{\mathbf{k}}} \sum_{\mathbf{k}, \mathbf{b}} w_{\mathbf{b}} \text{Im}\{\ln M_{nn}^{\mathbf{k}, \mathbf{b}}\} \mathbf{b}. \quad (2.50)$$

With these expressions at hand, it is possible to systematically investigate the spread Ω with the goal of finding a set of unitary transformations $U^{\mathbf{k}}$ which eventually yield a

small value for Ω . In the following, three different approaches of such a procedure, that have been reported in the literature and which are implemented in the present work, are introduced.

2.5. Construction of Wannier functions

2.5.1. The projection method

A computationally cheap and very simple way to approach a set of transformations $U^{\mathbf{k}}$ leading to localized WFs is the so-called projection method. This method finds its inspiration in the work of Cloizeaux [Clo64] and discussed e.g. in Ref. [MV97]. It aims to generate $U^{\mathbf{k}}$ from a set of guess functions of the J WFs in the home unit cell. We take a set of J trial orbitals $g_n(\mathbf{r})$ that should roughly describe the position and the angular character of the resulting WFs. We start by computing their projection on the original J Bloch states in the considered subspace

$$A_{mn}^{\mathbf{k}} = \langle m\mathbf{k} | g_n \rangle^{\text{SC}} . \quad (2.51)$$

Using $A^{\mathbf{k}}$, we construct auxiliary mixed Bloch states

$$\phi_{n,\mathbf{k}}(\mathbf{r}) = \sum_{m=1}^J A_{mn}^{\mathbf{k}} \Psi_{m,\mathbf{k}}(\mathbf{r}) , \quad (2.52)$$

and orthonormalize them using Löwdin's procedure [Löw50], namely,

$$\psi_{n,\mathbf{k}}(\mathbf{r}) = \sum_{m=1}^J (S^{\mathbf{k}-1/2})_{mn} \phi_{m,\mathbf{k}}(\mathbf{r}) , \quad (2.53)$$

where $S^{\mathbf{k}} = A^{\mathbf{k}\dagger} A^{\mathbf{k}}$ denotes the overlap matrix of the $\phi_{n,\mathbf{k}}$. Comparing Eq. (2.53) to Eq. (2.33) we identify

$$U^{\mathbf{k}} = A^{\mathbf{k}} (A^{\mathbf{k}\dagger} A^{\mathbf{k}})^{-1/2} . \quad (2.54)$$

The $U^{\mathbf{k}}$ defined this way is the closest unitary approximation of $A^{\mathbf{k}}$. In practice, it is calculated by performing a singular value decomposition of $A^{\mathbf{k}} = V \Sigma W^\dagger$, where V and W are unitary and $\Sigma = \text{diag}\{\sigma_1, \sigma_2, \dots, \sigma_J\}$ is real and diagonal with the non-negative singular values σ_i . Then, $U^{\mathbf{k}} = V W^\dagger$.

For some simple cases, e.g. the four isolated valence bands in silicon, this basic approach yields well localized WFs that can be used for further applications. However, the simple projection method solely depends on the projection functions g_n and the resulting WFs are sensitive to them. It limits the applicability of this approach to more complex systems and applications, where strongly localized WFs are required. Nevertheless, this procedure serves well as a basic starting point for more elaborated methods.

2.5.2. Optimized projection functions

Following Ref. [Mus+15], we systematically extend the simple projection method. We start from a larger set of $K \geq J$ trial orbitals $g_m(\mathbf{r})$ and aim at finding J linear combinations

$$\tilde{g}_n(\mathbf{r}) = \sum_{m=1}^K B_{mn} g_m(\mathbf{r}), \quad n = 1, \dots, J, \quad (2.55)$$

that eventually give the most localized WFs after using them as projection functions in the simple projection method. The K functions $g_n(\mathbf{r})$ should be chosen such that they span a space that includes the subspace of the J WFs (or equivalent the space spanned by the J original Bloch states $\Psi_{n,\mathbf{k}}$). Mustafa and coworkers [Mus+15] developed an algorithm to find the rectangular semi-unitary $K \times J$ matrix B that minimizes the spread Ω . Since the \tilde{g}_n minimize Ω within the subspace spanned by the g_n they are called optimized projection functions (OPFs).

Like in the simple projection, we start by calculating the (rectangular) overlap matrices $A^{\mathbf{k}}$ according to Eq. (2.51). Then, the (square) overlaps with the OPFs read

$$\tilde{A}^{\mathbf{k}} = A^{\mathbf{k}} B, \quad (2.56)$$

and we yield

$$\tilde{U}^{\mathbf{k}} = A^{\mathbf{k}} B (B^\dagger A^{\mathbf{k}\dagger} A^{\mathbf{k}} B)^{-1/2} \quad (2.57)$$

for the transformation matrices obtained from the OPFs (see Eq. (2.54)). In order to minimize Ω with respect to B , Mustafa and coworkers [Mus+15] made a few simplifications. First, $B^\dagger A^{\mathbf{k}\dagger} A^{\mathbf{k}} B$ is considered to be close to the identity matrix and the inverse

square root in Eq. (2.57) is Taylor expanded in the vicinity of $\mathbb{1}_J$ and truncated at the lowest order

$$\begin{aligned}\tilde{U}^{\mathbf{k}} &= A^{\mathbf{k}}B \left(B^\dagger A^{\mathbf{k}\dagger} A^{\mathbf{k}}B \right)^{-1/2} \\ &= A^{\mathbf{k}}B \left[\mathbb{1}_J - \frac{1}{2} \left(B^\dagger A^{\mathbf{k}\dagger} A^{\mathbf{k}}B - \mathbb{1}_J \right) + \dots \right] \\ &\approx A^{\mathbf{k}}B .\end{aligned}\tag{2.58}$$

Moreover, to restore unitarity, the rectangular overlap matrix $A^{\mathbf{k}}$ is replaced by its closest semi-unitary approximation $U^{\mathbf{k}}$ (compare Eq. (2.54)), and we arrive at a unitary approximation for $\tilde{U}^{\mathbf{k}}$

$$\tilde{U}^{\mathbf{k}} \approx U^{\mathbf{k}}B .\tag{2.59}$$

Second, Ω can be replaced by $\Omega_{\text{I}} + \Omega_{\text{OD}}$ when minimizing it with respect to B . Mustafa and coworkers [Mus+15] argued that the diagonal part Ω_{D} (Eq. (2.37)) is negligible close to maximal localization, since the $\mathbf{R} = \mathbf{0}$ term will dominate in Eqs. (2.36) - (2.38) due to the exponential localization of WFs. Applying these two simplifications and using the reciprocal-space representation of Ω_{I} in Eq. (2.42) and Ω_{OD} in Eq. (2.44), Mustafa and coworkers [Mus+15] formulated a target Lagrangian

$$\mathcal{L}(B, \lambda) = - \sum_{\mathbf{k}, \mathbf{b}} w_{\mathbf{b}} \sum_{n=1}^J \left| \left[B^\dagger U^{\mathbf{k}\dagger} \mathcal{M}^{\mathbf{k}, \mathbf{b}} U^{\mathbf{k}+\mathbf{b}} B \right]_{nn} \right|^2 + \lambda w \sum_{\mathbf{k}} \sum_{n=1}^J \left| \left[B^\dagger A^{\mathbf{k}\dagger} A^{\mathbf{k}} B \right]_{nn} - 1 \right|^2 ,\tag{2.60}$$

where the second term includes the assumption made in Eq. (2.58) as a constraint with the Lagrange multiplier λ and $w = \sum_{\mathbf{b}} w_{\mathbf{b}}$. Now, the problem of finding OPFs is equivalent to finding a rectangular, semi-unitary matrix B and a real number λ that minimize \mathcal{L} . In practice, this is done by keeping λ fixed at some value (e.g. $\lambda = 1$) and updating B by successive applications of Givens rotations [Bjö96]. A detailed description of this procedure is available in Appendix A of Ref. [Mus+15].

2.5.3. Maximally localized Wannier functions

While the projection method is cheap, it strongly depends on the choice of projection functions and requires a quite good guess of the expected WFs. This deficiency is cured partially by calculating OPFs. In order to develop an algorithm that is more robust and also applicable to large subspaces of several dozens bands, one needs to tackle the

problem of finding suitable $U^{\mathbf{k}}$ more systematically. Therefore, Marzari and Vanderbilt [MV97] developed an iterative procedure to minimize the spread Ω with respect to the transformation matrices $U^{\mathbf{k}}$. The minimization is done by successively applying small unitary rotations $d\mathbb{1}^{\mathbf{k}} = \exp\{dW^{\mathbf{k}}\}$ to the transformations $U^{\mathbf{k}}$, where anti-Hermiticity, i.e. $dW^{\mathbf{k}} = -dW^{\mathbf{k}\dagger}$, is imposed to ensure that $d\mathbb{1}^{\mathbf{k}}$ is unitary. Replacing $U^{\mathbf{k}} \rightarrow U^{\mathbf{k}}d\mathbb{1}^{\mathbf{k}}$ results in a small change $d\Omega$ of the spread functional. Following the derivation of Marzari and Vanderbilt [MV97], we express the gradient of Ω with respect to small variations $dW^{\mathbf{k}}$

$$G_{mn}^{\mathbf{k}} := \frac{\partial\Omega}{\partial\overline{W_{mn}^{\mathbf{k}}}} = 4 \sum_{\mathbf{b}} w_{\mathbf{b}} \left(\mathcal{S}[T^{\mathbf{k},\mathbf{b}}]_{mn} - \mathcal{A}[R^{\mathbf{k},\mathbf{b}}]_{mn} \right), \quad (2.61)$$

with $\mathcal{S}[X] = (X + X^\dagger)/2i$ and $\mathcal{A}[X] = (X - X^\dagger)/2$ as well as

$$R_{mn}^{\mathbf{k},\mathbf{b}} = M_{mn}^{\mathbf{k},\mathbf{b}} \overline{M_{nn}^{\mathbf{k},\mathbf{b}}}, \quad (2.62)$$

and

$$T_{mn}^{\mathbf{k},\mathbf{b}} = \frac{M_{mn}^{\mathbf{k},\mathbf{b}}}{M_{nn}^{\mathbf{k},\mathbf{b}}} \left(\text{Im}\{\ln M_{nn}^{\mathbf{k},\mathbf{b}}\} + \mathbf{b} \cdot \langle \mathbf{r} \rangle_n \right). \quad (2.63)$$

Note, that in contrast to Ref. [MV97], we define $G^{\mathbf{k}}$ as the derivative with respect to the complex conjugate $\overline{dW^{\mathbf{k}}}$ instead of $dW^{\mathbf{k}}$ and it holds

$$\frac{\partial\Omega}{\partial\overline{W_{mn}^{\mathbf{k}}}} = -\frac{\partial\Omega}{\partial W_{nm}^{\mathbf{k}}} = -\left(\frac{\partial\Omega}{\partial W^{\mathbf{k}}} \right)_{mn}. \quad (2.64)$$

Defined in that way, $G^{\mathbf{k}}$ indicates the direction of maximum increase of Ω . Now, once the gradient $G^{\mathbf{k}}$ is known, successive small updates in a direction $P^{\mathbf{k}}$ of decreasing Ω can be applied to the transformations $U^{\mathbf{k}}$. Therefore we use

$$dW^{\mathbf{k}} = \frac{\mu}{4w} P^{\mathbf{k}}, \quad (2.65)$$

where μ is the step length for the update. In their original work, Marzari and Vanderbilt [MV97] suggested a simple steepest-descent approach where the negative direction of the gradient was chosen as the update direction

$$P^{\mathbf{k}} = -G^{\mathbf{k}}, \quad (2.66)$$

and μ was set to be a fixed step length. Once $dW^{\mathbf{k}}$ is calculated, the matrices $U^{\mathbf{k}}$ and $M^{\mathbf{k},\mathbf{b}}$ are updated according to

$$U^{\mathbf{k}} \rightarrow U^{\mathbf{k}} \exp\{dW^{\mathbf{k}}\} \quad (2.67)$$

and Eq. (2.47), respectively. Note, that $G^{\mathbf{k}}$ is anti-Hermitian and thus a valid update direction. For the calculation of the matrix exponential, we diagonalize $idW^{\mathbf{k}}$ (which is Hermitian) with a standard solver for Hermitian matrices. This procedure of calculating the gradient, finding the update direction and updating the transformation matrices then is repeated until convergence of Ω is reached. Assuming a sufficiently good starting point, this algorithm reaches the global minimum of Ω and the resulting WFs are called maximally localized (with respect to the used localization criterion).

Each update involves relatively inexpensive matrix-matrix multiplications and a diagonalization of a small Hermitian matrix, while the more expensive calculation of the plane wave matrix elements in Eq. (2.48) just needs to be done once in advance.

2.6. Wannier interpolation

Many quantities such as the dielectric function involve integrals over the BZ which require a dense sampling in order to achieve the desired accuracy. Usually, these integrations come along with significantly high computational effort which limits the feasible number of \mathbf{k} -points. In this case, a scheme that accurately interpolates quantities obtained on a coarse \mathbf{k} -mesh in reciprocal-space is desired. There are several alternative theories addressing this problem, e.g. Shirley's interpolation scheme ([Shi96; PL09]) or $\mathbf{k} \cdot \mathbf{p}$ perturbation theory ([LKW55; Kan56; PA07]). Here, we focus on the Wannier interpolation scheme. The basic idea of Wannier interpolation is to calculate an optimal tight-binding basis consisting of well localized functions starting from Bloch waves (that are obtained using DFT and methods beyond) on a coarse supporting \mathbf{k} -grid. This tight-binding basis is usually much smaller than the original one in which the wavefunctions are expanded (e.g. plane waves or APWs). From this basis, a \mathbf{k} -dependent Hamiltonian matrix for an arbitrary point \mathbf{q} in reciprocal-space is constructed using the Slater–Koster interpolation scheme [SK54], and its diagonalization yields the interpolated eigenenergies and wavefunctions expressed in the tight-binding basis. From this eigensystem, a variety of derived quantities such as band energies or partial densities can be interpolated in reciprocal-space. In the

following, \mathbf{k} labels a point on the supporting (coarse) mesh and \mathbf{q} labels an arbitrary point in reciprocal-space for which an interpolation is made. In particular, \mathbf{q} may be part of a finer interpolation grid or a point along a specific path through the BZ.

2.6.1. Interpolation of the wavefunction

In order to obtain the interpolated wavefunction, we first use the localized WFs for constructing a set of auxiliary Bloch waves $|\phi_{\mu,\mathbf{q}}\rangle$ for arbitrary \mathbf{q} . An inversion of Eq. (2.34) for \mathbf{q} instead of \mathbf{k} yields

$$|\phi_{\mu,\mathbf{q}}\rangle = \sum_{\mathbf{R}} e^{i\mathbf{q}\cdot\mathbf{R}} |\mu\mathbf{R}\rangle . \quad (2.68)$$

The $|\phi_{\mu,\mathbf{q}}\rangle$ form the basis for expanding the interpolated wavefunctions

$$|m\mathbf{q}\rangle = \sum_{\mu} V_{\mu m}^{\mathbf{q}} |\phi_{\mu,\mathbf{q}}\rangle , \quad (2.69)$$

where $V_{\mu m}^{\mathbf{q}}$ are expansion coefficients that are discussed further in Sec. 2.6.2. Note the similarity to the tight-binding formalism by comparing Eq. (2.68) with Eq. (2.16) and Eq. (2.69) with Eq. (2.17), respectively. Plugging in the definition of the WFs (Eq. (2.34)) and the mixed Bloch states (Eq. (2.33)) into Eqs. (2.68) and (2.69) yields an expression of the interpolated wavefunctions in terms of the given wavefunctions on the original \mathbf{k} -grid

$$|m\mathbf{q}\rangle = \sum_{\mu} V_{\mu m}^{\mathbf{q}} \sum_{\mathbf{R}} e^{i\mathbf{q}\cdot\mathbf{R}} \frac{1}{N_{\mathbf{k}}} \sum_{\mathbf{k}} e^{-i\mathbf{k}\cdot\mathbf{R}} \sum_{\nu} U_{\nu\mu}^{\mathbf{k}} |\nu\mathbf{k}\rangle . \quad (2.70)$$

In practice, this expression is shortened by introducing the phase matrix \mathcal{P}

$$|m\mathbf{q}\rangle = \sum_{\mu} V_{\mu m}^{\mathbf{q}} \sum_{\mathbf{k}} \mathcal{P}_{\mathbf{k}\mathbf{q}} \sum_{\nu} U_{\nu\mu}^{\mathbf{k}} |\nu\mathbf{k}\rangle , \quad (2.71)$$

$$\mathcal{P}_{\mathbf{k}\mathbf{q}} = \frac{1}{N_{\mathbf{k}}} \sum_{\mathbf{R}} e^{i(\mathbf{q}-\mathbf{k})\cdot\mathbf{R}} . \quad (2.72)$$

If the set of \mathbf{R} -vectors is chosen symmetrically centered around the origin (e.g. as outlined in Sec. 3.6.1), $\mathcal{P}_{\mathbf{k}\mathbf{q}}$ becomes real valued.

2.6.2. Interpolation of eigenenergies

We have seen from the previous section that whenever we want to compute the interpolated wavefunctions, and hence derived quantities (e.g. matrix elements), we need the expansion coefficients $V_{\mu m}^{\mathbf{q}}$. They are a side-product of the interpolation of the eigenenergies of the system. Therefore, the following interpolation step forms the initial basis operation for all further interpolations which may possibly be carried out. We follow the derivations outlined in [Mar+12]. In order to obtain the interpolated energies $\varepsilon_m^{\mathbf{q}}$ we need to calculate the Hamiltonian matrix elements in the interpolated wavefunctions. Obviously, this matrix should be diagonal (also referred to be in the *Hamiltonian gauge*) to accommodate the property of the $|m\mathbf{q}\rangle$ to be eigenfunctions of the Hamiltonian

$$H_{mn}^{\mathbf{q}} = \langle m\mathbf{q} | \hat{\mathbf{H}} | n\mathbf{q} \rangle^{\Omega_c} = \varepsilon_m^{\mathbf{q}} \delta_{mn} . \quad (2.73)$$

With Eq. (2.69) this expression reads

$$H_{mn}^{\mathbf{q}} = \sum_{\mu, \nu} \overline{V_{\mu m}^{\mathbf{q}}} \langle \phi_{\mu, \mathbf{q}} | \hat{\mathbf{H}} | \phi_{\nu, \mathbf{q}} \rangle^{\Omega_c} V_{\nu n}^{\mathbf{q}} , \quad (2.74)$$

or, in the matrix representation

$$H^{\mathbf{q}} = V^{\mathbf{q}\dagger} \mathcal{H}^{\mathbf{q}} V^{\mathbf{q}} , \quad (2.75)$$

where $\mathcal{H}_{\mu\nu}^{\mathbf{q}} = \langle \phi_{\mu, \mathbf{q}} | \hat{\mathbf{H}} | \phi_{\nu, \mathbf{q}} \rangle^{\Omega_c}$ denotes the Hamiltonian in the *Wannier gauge* which is not necessarily diagonal. The expansion coefficients $V_{\mu m}^{\mathbf{q}}$ play the role of the unitary transformations that diagonalize the Hamiltonian in the Wannier gauge. We now calculate

$$\mathcal{H}_{\mu\nu}^{\mathbf{q}} = \langle \phi_{\mu, \mathbf{q}} | \hat{\mathbf{H}} | \phi_{\nu, \mathbf{q}} \rangle^{\Omega_c} = \frac{1}{N_{\mathbf{k}}} \langle \phi_{\mu, \mathbf{q}} | \hat{\mathbf{H}} | \phi_{\nu, \mathbf{q}} \rangle^{\text{SC}} . \quad (2.76)$$

This is generally true for Bloch states and periodic operators with $\hat{\mathbf{O}}(\mathbf{r} + \mathbf{R}) = \hat{\mathbf{O}}(\mathbf{r})$, such as the Hamilton operator. By the use of Eq. (2.68) we obtain

$$\langle \phi_{\mu, \mathbf{q}} | \hat{\mathbf{H}} | \phi_{\nu, \mathbf{q}} \rangle^{\text{SC}} = \sum_{\mathbf{R}, \mathbf{R}'} e^{i\mathbf{q} \cdot (\mathbf{R}' - \mathbf{R})} \langle \mu \mathbf{R} | \hat{\mathbf{H}} | \nu \mathbf{R}' \rangle^{\text{SC}} . \quad (2.77)$$

Now we make use of the periodicity of the Hamiltonian and Eq. (2.26) and obtain

$$\begin{aligned}
\langle \mu \mathbf{R} | \hat{\mathbf{H}} | \nu \mathbf{R}' \rangle^{\text{SC}} &= \int_{\text{SC}} \overline{w_{\mu, \mathbf{R}}}(\mathbf{r}) \hat{\mathbf{H}}(\mathbf{r}) w_{\nu, \mathbf{R}'}(\mathbf{r}) d\mathbf{r} \\
&= \int_{\text{SC}} \overline{w_{\mu, \mathbf{0}}}(\mathbf{r} - \mathbf{R}) \hat{\mathbf{H}}(\mathbf{r}) w_{\nu, \mathbf{R}'}(\mathbf{r}) d\mathbf{r} \\
&= \int_{\text{SC}} \overline{w_{\mu, \mathbf{0}}}(\mathbf{r}) \hat{\mathbf{H}}(\mathbf{r} + \mathbf{R}) w_{\nu, \mathbf{R}'}(\mathbf{r} + \mathbf{R}) d\mathbf{r} \\
&= \int_{\text{SC}} \overline{w_{\mu, \mathbf{0}}}(\mathbf{r}) \hat{\mathbf{H}}(\mathbf{r}) w_{\nu, \mathbf{R}' - \mathbf{R}}(\mathbf{r}) d\mathbf{r} \\
&= \langle \mu \mathbf{0} | \hat{\mathbf{H}} | \nu \mathbf{R}' - \mathbf{R} \rangle^{\text{SC}} .
\end{aligned} \tag{2.78}$$

A rearrangement of the indices \mathbf{R} and \mathbf{R}' eventually gives the final result

$$\mathcal{H}_{\mu\nu}^{\mathbf{q}} = \langle \phi_{\mu, \mathbf{q}} | \hat{\mathbf{H}} | \phi_{\nu, \mathbf{q}} \rangle^{\Omega_c} = \sum_{\mathbf{R}} e^{i\mathbf{q} \cdot \mathbf{R}} \langle \mu \mathbf{0} | \hat{\mathbf{H}} | \nu \mathbf{R} \rangle^{\text{SC}} . \tag{2.79}$$

The matrix elements $\langle \mu \mathbf{0} | \hat{\mathbf{H}} | \nu \mathbf{R} \rangle^{\text{SC}}$ are calculated by Fourier-transforming Eq. (2.79) on the original \mathbf{k} -grid

$$\begin{aligned}
\langle \mu \mathbf{0} | \hat{\mathbf{H}} | \nu \mathbf{R} \rangle^{\text{SC}} &= \frac{1}{N_{\mathbf{k}}} \sum_{\mathbf{k}} e^{-i\mathbf{k} \cdot \mathbf{R}} \langle \phi_{\mu, \mathbf{k}} | \hat{\mathbf{H}} | \phi_{\nu, \mathbf{k}} \rangle^{\Omega_c} \\
&= \frac{1}{N_{\mathbf{k}}} \sum_{\mathbf{k}} e^{-i\mathbf{k} \cdot \mathbf{R}} \left[U^{\mathbf{k}\dagger} H^{\mathbf{k}} U^{\mathbf{k}} \right]_{\mu\nu} \\
&=: H_{\mu\nu}^{\mathbf{R}}
\end{aligned} \tag{2.80}$$

where, in the second line, we have made use of Eqs. (2.34) and (2.33) and $H_{mn}^{\mathbf{k}} = \epsilon_m^{\mathbf{k}} \delta_{mn}$ is the diagonal Hamiltonian on the support grid. We call $H^{\mathbf{R}}$ the real-space representation of the Hamiltonian which is independent of the interpolation points \mathbf{q} and therefore needs to be calculated just once for all \mathbf{R} in advance. The Hamiltonian in the Wannier gauge is then obtained by performing the inexpensive Fourier sum

$$\mathcal{H}^{\mathbf{q}} = \sum_{\mathbf{R}} e^{i\mathbf{q} \cdot \mathbf{R}} H^{\mathbf{R}} . \tag{2.81}$$

Alternatively it can be expressed as

$$\mathcal{H}^{\mathbf{q}} = \sum_{\mathbf{k}} \mathcal{P}_{\mathbf{k}\mathbf{q}} U^{\mathbf{k}\dagger} H^{\mathbf{k}} U^{\mathbf{k}} \quad (2.82)$$

by the use of Eqs. (2.80) and (2.79) with the known phase matrix \mathcal{P} (Eq. (2.72)). We obtain the interpolated eigenenergies $\epsilon_m^{\mathbf{q}}$ and the expansion coefficients $V_{\mu m}^{\mathbf{q}}$ by the diagonalization of $\mathcal{H}^{\mathbf{q}}$ for each point \mathbf{q} on the interpolation grid. Since $\mathcal{H}^{\mathbf{q}}$ has the dimension J of the band range, which is usually much smaller than the total basis size, this interpolation step is rather cheap and much faster than the diagonalization of the Hamiltonian in the full (L)APW+lo basis.

If the interpolation grid \mathbf{q} coincides with the coarse first-principle grid \mathbf{k} , the phase matrix becomes unity $\mathcal{P}_{\mathbf{k}\mathbf{q}} = \delta_{\mathbf{k}\mathbf{q}}$, and Eq. (2.82) reduces to $\mathcal{H}^{\mathbf{q}} = U^{\mathbf{q}\dagger} H^{\mathbf{q}} U^{\mathbf{q}}$. In this case, the diagonalization of $\mathcal{H}^{\mathbf{q}}$ simply reads $H^{\mathbf{q}} = U^{\mathbf{q}} \mathcal{H}^{\mathbf{q}} U^{\mathbf{q}\dagger}$ and we identify the expansion coefficients with $V^{\mathbf{q}} = U^{\mathbf{q}\dagger}$. The last equation is just determined up to an arbitrary phase factor for each column of $V^{\mathbf{q}}$. Furthermore, it becomes clear that the interpolation scheme reproduces the original eigenenergies $\epsilon_m^{\mathbf{k}}$ when \mathbf{q} is a vector of the original \mathbf{k} -grid.

3. Implementation

3.1. Workflow

All implementations and calculations are carried out within the full-potential all-electron code `exciting` [Gul+14]. Wavefunctions and eigenenergies calculated on the coarse \mathbf{k} -grid are obtained from the already existing code and used as the starting point for the generation of WFs and different interpolation quantities which are the subject of the present work.

In order to generate well-localized WFs, the single-particle wavefunctions $\Psi_{n,\mathbf{k}}(\mathbf{r})$ need to be provided. In our calculations, the latter ones stem either from KS-DFT calculations with local xc-potentials or from calculations using non-local hybrid xc-potentials. The overall workflow of the present implementation is depicted in Fig. 3.1.

In the first step of the Wannierization procedure (indicated by a yellow bar in Fig. 3.1), the preparation of all quantities, that are necessary to compute a first set of transformation matrices $U^{\mathbf{k}}$, is carried out. In particular, these are the overlaps between the wavefunctions and the projection functions $A^{\mathbf{k}}$ (Eq. (2.51)) which are required in all cases and, optionally, the plane wave matrix elements $\mathcal{M}^{\mathbf{k},\mathbf{b}}$ (Eq. (2.48)). The latter ones do not need to be calculated if one wants to generate the $U^{\mathbf{k}}$ using the simple projection method. Often – especially for large systems, dense \mathbf{k} -grids or large band-ranges – calculating $\mathcal{M}^{\mathbf{k},\mathbf{b}}$ forms the most expensive and time consuming part, hence, it should be implemented most efficiently. In Appendix A, it is shown how the matrix elements are calculated within the (L)APW+lo basis. This preparation phase is the only part in the generation of WFs that depends on the wavefunctions and the used projection functions. Once the $A^{\mathbf{k}}$ and $\mathcal{M}^{\mathbf{k},\mathbf{b}}$ are calculated, the remaining steps (besides possible interpolations) are independent of the explicit wavefunctions. Thus, the entire procedure can easily be adapted to input calculations stemming from more elaborated methods compared to KS-DFT, e.g. the self-consistent *GW* method.

The second step (blue bar in Fig. 3.1) provides a first set of transformation matrices $U^{\mathbf{k}}$. These are computed either directly from the overlaps $A^{\mathbf{k}}$ using the simple projection approach or from projection on OPFs. In the latter case, the matrix B in Eq. (2.55), that determines the OPFs, has to be calculated. In principle, the transformations obtained that way can be used to explicitly calculate WFs from them which are then used for further applications. In practice, however, this first set of $U^{\mathbf{k}}$ usually serves as an initial

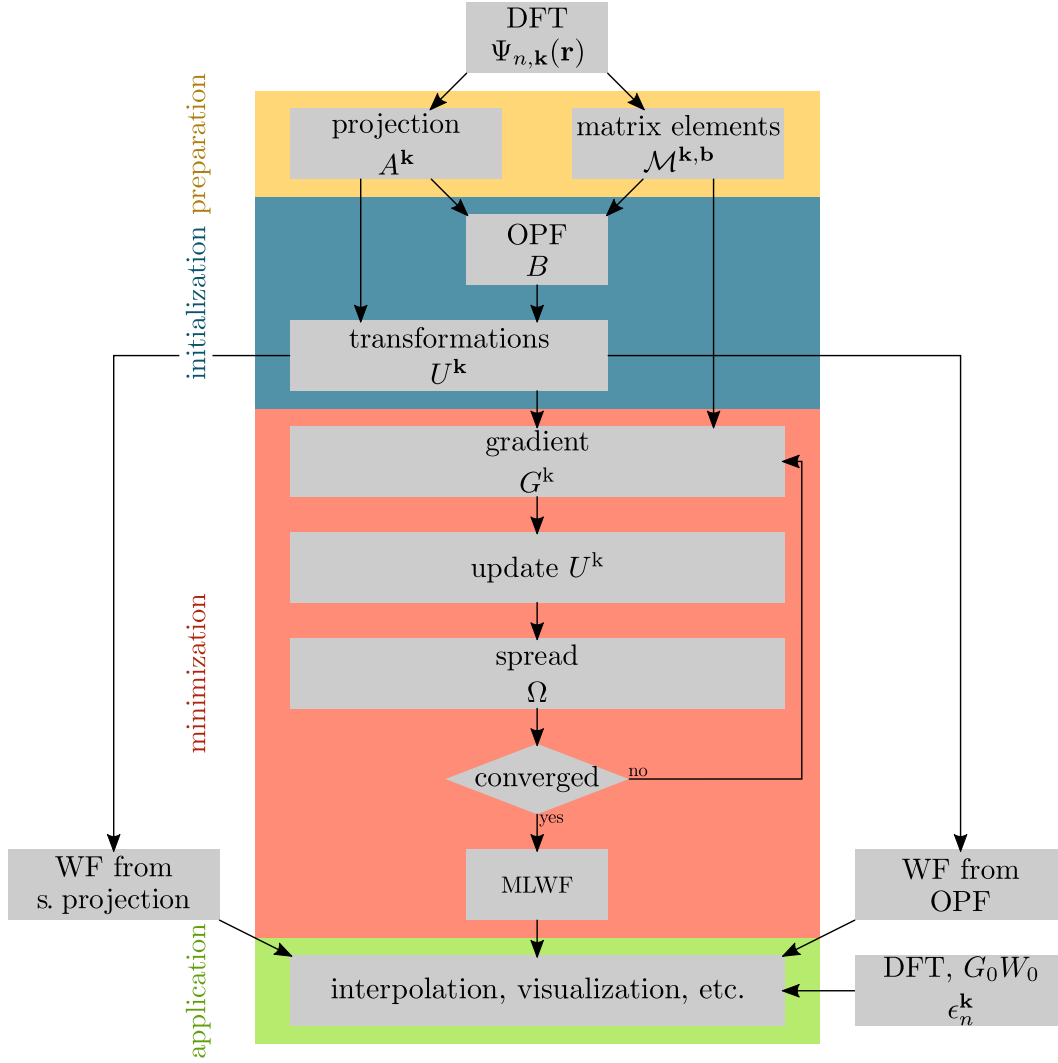


Fig. 3.1: Flowchart of the Wannierization procedure

guess for the calculation of MLWFs. Therefore, we call this second step the initialization phase.

The third step (red bar in Fig. 3.1) is optional but in practice usually conducted. It involves the iterative minimization of the gauge dependent part of the spread Ω (Eqs. (2.43), (2.44)). First, the gradient $G^{\mathbf{k}}$ (Eq. (2.61)) is calculated using $\mathcal{M}^{\mathbf{k},\mathbf{b}}$ and the initial $U^{\mathbf{k}}$. Then, the transformations are updated according to Eq. (2.67), and the new spread Ω is computed. These steps are repeated until a given convergence criterion is fulfilled. The result of this phase is a set of transformations $U^{\mathbf{k}}$ that represent MLWFs.

Usually, one is not interested in the bare transformations $U^{\mathbf{k}}$ but wants to use them for further applications such as the visualization of WFs or the interpolation of different quantities. All these possible applications make up the fourth step (green bar in Fig. 3.1). In order to use the computed WFs (or more precisely the set of unitary transformations) for interpolations, the eigenenergies $\epsilon_n^{\mathbf{k}}$ are additionally required. In the calculations within this work, these are either (generalized) KS eigenenergies or quasi-particle energies obtained within the G_0W_0 approximation. The eigensystem interpolation then provides the interpolated energies $\epsilon_n^{\mathbf{q}}$ and the matrices $V^{\mathbf{q}}$ that are necessary to describe the expansion of the interpolated wavefunctions in Eq. (2.70).

3.2. Projection and choice of projection functions

Both methods described in Sec. 2.5, the simple projection and the projection on OPFs, require a set of localized guess functions that roughly describe the shape and position of the WFs. Hence, it is crucial to choose them wisely since they strongly determine the quality and usability of the obtained WFs and their further application. In this work, we employ local orbitals introduced in Sec. 2.3. They are strongly localized by definition since they are strictly zero outside the MT of one specific atom. Furthermore, they fit the specific problem at hand since their radial functions satisfy the radial Schrödinger equation for the averaged spherically symmetric potential of the nucleus inside the MT. And, finally, the form of a radial function times a spherical harmonic and the fact that the local orbitals are part of the basis set in which the KS equations are solved, significantly simplifies the calculation of the projection overlap matrix $A^{\mathbf{k}}$ since all the required radial integrals are already available. However, the local orbitals as projection functions have drawbacks. For instance, we find local orbitals being unsuitable guesses in cases where the MLWFs we are aiming at are located in between different atoms rather than on atomic sites. Here, functions that are strictly atom centered and zero in the interstitial region are impractical for the expansion of an initial guess of the WFs. In the (L)APW+lo

framework, the overlap (entries of the matrices $A^{\mathbf{k}}$) between a KS wavefunction and a local orbital $\phi_{\mathbf{L}}$ with angular quantum numbers $l_{\mathbf{L}}$ and $m_{\mathbf{L}}$ centered at atom $\alpha_{\mathbf{L}}$ reads

$$\begin{aligned} \langle \Psi_{n,\mathbf{k}} | \phi_{\mathbf{L}} \rangle &= \sum_{\mathbf{G}+\mathbf{k}} \sum_o C_{n,\mathbf{G}}^{\mathbf{k}} A_{l_{\mathbf{L}}m_{\mathbf{L}},o,\mathbf{G}+\mathbf{k}}^{\alpha_{\mathbf{L}}} \int_{\text{MT}_{\alpha_{\mathbf{L}}}} r^2 u_{l_{\mathbf{L}},o}^{\alpha_{\mathbf{L}}}(r) f_{l_{\mathbf{L}}}^{\mathbf{L}}(r) dr \\ &+ \sum_{\mathbf{L}'} C_{n,\mathbf{L}'}^{\mathbf{k}} \int_{\text{MT}_{\alpha_{\mathbf{L}}}} r^2 f_{l_{\mathbf{L}'}}^{\mathbf{L}'}(r) f_{l_{\mathbf{L}}}^{\mathbf{L}}(r) dr \delta_{\alpha_{\mathbf{L}'},\alpha_{\mathbf{L}}} \delta_{l_{\mathbf{L}'},l_{\mathbf{L}}} \delta_{m_{\mathbf{L}'},m_{\mathbf{L}}} , \end{aligned} \quad (3.1)$$

where $u_{l_{\mathbf{L}},o}^{\alpha_{\mathbf{L}}}(r)$ is an (L)APW radial function with matching order o and $f_{l_{\mathbf{L}'}}^{\mathbf{L}'}(r)$ are the radial functions of the local orbitals.

3.3. Initial guess from simple projection

The simple projection method is by far the cheapest approach since it just requires the calculation of the projection matrices $A^{\mathbf{k}}$ and a singular value decomposition of them. For the cases studied, this is a matter of a few seconds for simple materials such as bulk silicon or a couple of minutes for much more complex compounds (e.g. molecular crystals) on a desktop computer. However, this approach is practical just for a limited number of situations. We find that the projection method works well and produce WFs usable for further interpolations for small isolated groups of bands (e.g. the valence bands in group IV-semiconductors). In Fig. 3.2 we show two sets of possible WFs for the four valence bands of silicon carbide in the zincblende structure calculated on $6 \times 6 \times 6$ sampling points in the BZ. One set is obtained by projecting the wavefunctions on one s - and three p -orbitals centered at the carbon atom. This yields four WFs with a combined spread of $\Omega = 6.114 \text{ \AA}^2$. In the second case, the projection is performed on one s - and three p -orbitals centered at the silicon atom resulting in less localized functions with $\Omega = 10.816 \text{ \AA}^2$. In both cases, the WFs clearly reflect the s - and p -characters of the used projection functions.

Although being not maximally localized, both sets of WFs are suited well for interpolating energies of the valence bands. In order to quantify the quality of the results, we compare the interpolated values with the values that are calculated using KS-DFT along a given test path through the BZ. This path passes through all inequivalent edges and face- and space-diagonals of the parallelepiped spanned by the reciprocal lattice vectors.

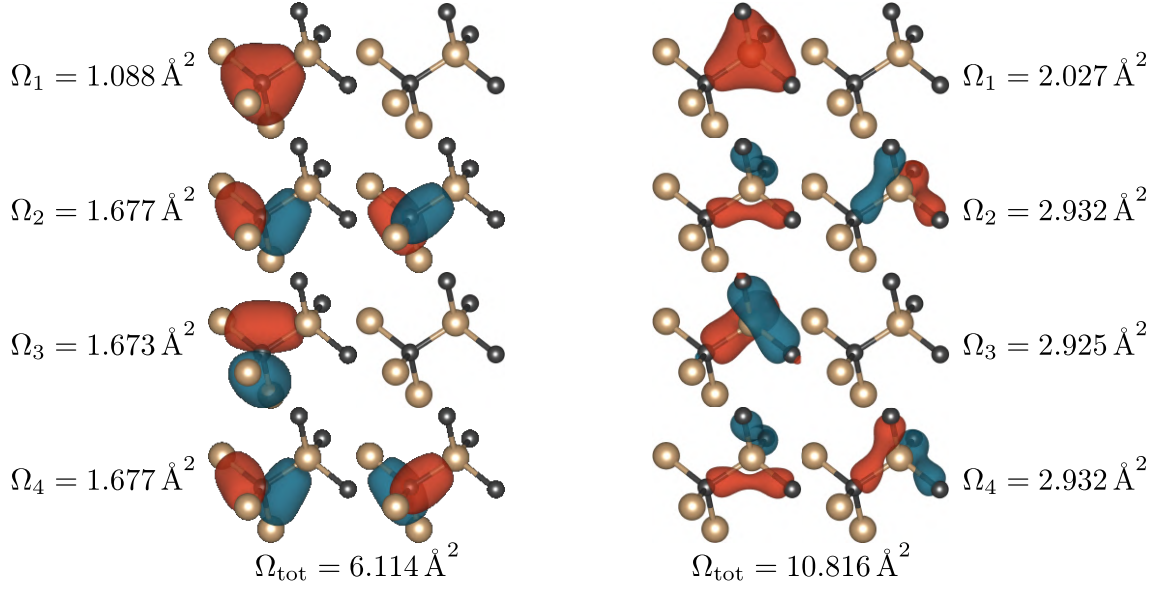


Fig. 3.2: WFs in SiC from simple projection on carbon and silicon s - and p -orbitals
 WFs for the four valence bands in silicon carbide are displayed along with their spreads Ω . They are obtained by simple projection on one s - and three p -orbitals centered on a carbon atom (black, left panel) and a silicon atom (gold, right panel), respectively. The real and imaginary parts of the function are shown in the left and right column of both panels.

As a measure of the interpolation quality we choose the root mean square (RMS) of the differences between the calculated energies ϵ_n^k and the interpolated energies ε_n^k

$$\delta\varepsilon_{\text{RMS}} = \sqrt{\frac{1}{JN} \sum_{n=1}^J \sum_{k=1}^N (\epsilon_n^k - \varepsilon_n^k)^2}, \quad (3.2)$$

where n is the band index and N is the number of equidistant sampling points along the path. Here and in all following cases we set $N = 3000$. In the current example, we obtain $\delta\varepsilon_{\text{RMS}} = 11.5$ meV for the projection on carbon and $\delta\varepsilon_{\text{RMS}} = 70.6$ meV for the projection on silicon. That means that the energy of a band within the considered subspace at an arbitrary \mathbf{k} -point can be predicted by Wannier interpolation using the given WFs in average up to this accuracy. This prediction is already fairly accurate considering that the four bands range over an interval of about 16 eV. However, the difference in the prediction accuracy for both sets is in accordance with the smaller spread of the WFs obtained from the carbon projection. Moreover, the functions depicted in the right panel of Fig. 3.2 avoid the silicon atom and tend towards the surrounding carbons while the functions on

the left are well attached to the carbon atom. It also indicates that in this particular case carbon-centered projection functions are more suitable.

Notably, the simple projection approach works well in this test case because we use physically justified projection functions. The four valence bands under consideration mainly originate from sp hybridized electrons, especially stemming from carbon. Therefore a projection on carbon s - and p -orbitals is the most appropriate choice here. The prediction quality and the spread significantly change when choosing different projection functions. A projection on four carbon d -orbitals for instance leads to a spread of $\Omega = 46.72 \text{ \AA}^2$ and $\delta\varepsilon_{\text{RMS}} = 395 \text{ meV}$ and even a projection on one s - and p -orbital centered at carbon and two p -orbitals centered at silicon gives $\Omega = 22.98 \text{ \AA}^2$ and $\delta\varepsilon_{\text{RMS}} = 241 \text{ meV}$. This reveals the major drawback of this approach that hinders it from being generally applicable. The simple projection method requires distinct knowledge of the nature of the bands under consideration and problem-adapted projection functions. This is usually no longer possible for more complex systems with still unknown electronic structures or larger band ranges of several dozens or hundreds of bands. Therefore, this method is hardly usable for practical applications.

3.4. Initial guess from OPFs

The cost of calculating OPFs can be significantly reduced by exploiting the symmetry of the matrix elements $\mathcal{M}^{\mathbf{k},\mathbf{b}}$ when the BZ is sampled using a Monkhorst–Pack \mathbf{k} -mesh [MP76]. Then, the \mathbf{k} -points form a Bravais lattice and therefore, whenever \mathbf{b} points to a neighbor of \mathbf{k} used in the finite-difference expression of the gradient, its opposite $-\mathbf{b}$ points to an equal neighbor with the same geometric weight $w_{\mathbf{b}}$. The plane wave matrix elements transform under inversion of \mathbf{b} as follows

$$\mathcal{M}^{\mathbf{k},-\mathbf{b}} = \mathcal{M}^{\mathbf{k}-\mathbf{b},\mathbf{b}^\dagger} . \quad (3.3)$$

This property also holds for the transformed matrix elements $M^{\mathbf{k},\mathbf{b}} = U^{\mathbf{k}\dagger} \mathcal{M}^{\mathbf{k},\mathbf{b}} U^{\mathbf{k}+\mathbf{b}}$. Making use of this symmetry, it is sufficient to perform the relatively expensive calculation of the matrix elements just for the 'positive' hemisphere \mathbf{b}_+ of the neighborhood shell, and the values for $-\mathbf{b}$ are given by the complex conjugate transpose of the matrix elements

at the reciprocal-space point $\mathbf{k} - \mathbf{b}$. We now reformulate the \mathbf{b} -dependent part of the Lagrangian in Eq. (2.60) and express it as

$$\begin{aligned} \sum_{\mathbf{k}, \mathbf{b}} w_{\mathbf{b}} \sum_{n=1}^J \left| [B^\dagger U^{\mathbf{k}\dagger} \mathcal{M}^{\mathbf{k}, \mathbf{b}} U^{\mathbf{k}+\mathbf{b}} B]_{nn} \right|^2 = \\ \sum_{\mathbf{b}_+} w_{\mathbf{b}} \sum_{n=1}^J \left(\sum_{\mathbf{k}} \left| [B^\dagger U^{\mathbf{k}\dagger} \mathcal{M}^{\mathbf{k}, \mathbf{b}} U^{\mathbf{k}+\mathbf{b}} B]_{nn} \right|^2 + \sum_{\mathbf{k}} \left| [B^\dagger U^{\mathbf{k}-\mathbf{b}\dagger} \mathcal{M}^{\mathbf{k}-\mathbf{b}, \mathbf{b}} U^{\mathbf{k}} B]_{nn} \right|^2 \right). \end{aligned} \quad (3.4)$$

Here, the two summations over \mathbf{k} give exactly the same contribution, and minimizing Eq. (2.60) w.r.t. B is equivalent to the minimization of

$$\mathcal{L}(B, \lambda) = -2 \sum_{\mathbf{k}, \mathbf{b}_+} w_{\mathbf{b}} \sum_{n=1}^J \left| [B^\dagger U^{\mathbf{k}\dagger} \mathcal{M}^{\mathbf{k}, \mathbf{b}} U^{\mathbf{k}+\mathbf{b}} B]_{nn} \right|^2 + \lambda w \sum_{\mathbf{k}} \sum_{n=1}^J \left| [B^\dagger A^{\mathbf{k}\dagger} A^{\mathbf{k}} B]_{nn} - 1 \right|^2. \quad (3.5)$$

The computing time of this slightly adapted problem is reduced by a factor of 1.75 in the case of six nearest neighbors (e.g. simple cubic) up to 1.86 for the triclinic case with 12 nearest neighbors. In total, the calculation of the OPF matrix B scales as $\mathcal{O}(N_{\mathbf{k}}(1 + N_{\mathbf{b}})JK)$ with the number of \mathbf{k} -points $N_{\mathbf{k}}$, the number of (symmetry reduced) neighbors $N_{\mathbf{b}}$, the number of bands J and the number of projection functions K .

Mustafa and coworkers [Mus+15] had reported their algorithm to be very robust against variations of the Lagrange multiplier λ in Eq. (2.60). We confirm this finding only partially. While the suggested default, $\lambda = 1$, usually works fine, there are a few test cases where λ has to be varied in order to achieve a sufficient localization for subsequent applications. For instance, in the above introduced example of the valence bands in silicon carbide, we have to use $\lambda = 10$ in order to obtain well-localized WFs. In contrast, we cannot reproduce the strong localization and similarity of the WFs obtained from OPFs to the MLWFs at the global minimum that was presented in Ref. [Mus+15]. They obtained WFs that were off the global minimum by just 1% in terms of the spread Ω , at least for isolated groups of bands. This discrepancy between our work and Ref. [Mus+15] may be caused by the different choice of projection functions (as discussed in Sec.3.2). Another significant inconsistency w.r.t Ref. [Mus+15] is that we do not include projections on orbitals in neighboring unit-cells, which leads to bad results when the centers of the MLWFs are close to the unit-cell boundary. Therefore, we did not use the OPF method as a stand-alone procedure. Even though we are not able to reproduce the promising results given in the original work, we find the OPF method to provide good starting points

for a further minimization using the approach given by Marzari and Vanderbilt [MV97]. In particular when considering large ranges of entangled bands, it becomes difficult to guess suitable functions for the projection, while the OPF method produces a reasonable initial guess. In our implementation, we consider the rectangular matrix B representing the OPFs to be converged when the Lagrangian \mathcal{L} varies by less than 1% between two consecutive sweeps. Hereby, one sweep is defined by a single update of each entry in the matrix B .

3.5. Minimization of the spread Ω

3.5.1. Conjugate gradient and line-search

The steepest descent approach with fixed step-length outlined in Ref. [MV97] can easily be extended to more sophisticated minimization procedures that just require the gradient, e.g. conjugate gradient (CG) methods with an additional line search for the optimal step length μ . In this work, a CG and a line-search algorithm have been implemented in order to minimize the spread Ω . Instead of using the negative gradient as the update direction P_i^k , an additional term containing the minimization algorithm's memory from the previous steps is appended

$$P_i^k = -G_i^k + \beta_i P_{i-1}^k, \quad (3.6)$$

where i counts the iterations and β labels the so called CG update parameter. The updates of the transformation matrices are still performed according to Eq. (2.67). In this work, different update parameters β has been implemented:

- the steepest descent (SD) method (no CG)

$$\beta_i^{\text{SD}} := 0,$$

- the *Hestenes–Stiefel* (HS) method [HS52]

$$\beta_i^{\text{HS}} := \frac{\text{Re}\{\langle G_i - G_{i-1}; G_i \rangle\}}{\text{Re}\{\langle G_i - G_{i-1}; P_{i-1} \rangle\}},$$

- the *Polák–Ribière* (PR) method [PR69]

$$\beta_i^{\text{PR}} := \frac{\text{Re}\{\langle G_i - G_{i-1}; G_i \rangle\}}{\langle G_{i-1}; G_{i-1} \rangle},$$

- and the *Fletcher–Reeves* (FR) method [FR64]

$$\beta_i^{\text{FR}} := \frac{\langle G_i; G_i \rangle}{\langle G_{i-1}; G_{i-1} \rangle}.$$

Here, the dot product $\langle G; P \rangle$ is defined as

$$\langle G; P \rangle := \sum_{\mathbf{k}} \sum_{m,n=1}^J \overline{G_{mn}^{\mathbf{k}}} P_{mn}^{\mathbf{k}} = \sum_{\mathbf{k}} \text{tr}\{G^{\mathbf{k}\dagger} P^{\mathbf{k}}\}. \quad (3.7)$$

In all cases, we use a modified update parameter $\beta_i^{(\cdot)+} = \max\{\beta_i^{(\cdot)}, 0\}$ which ensures an automatic reset of the algorithm whenever $\beta_i^{(\cdot)}$ becomes negative. A reset means that the algorithm loses its memory and restarts searching in the direction of the steepest descent. However, these CG methods perform best in combination with an accurate line search. It means, once the search direction $P_i^{\mathbf{k}}$ is determined, the step length μ_i that minimizes Ω in the direction of $P_i^{\mathbf{k}}$ needs to be found. Therefore, we consider the function

$$\Omega(\mu_i) := \Omega \left[\left\{ U_{i-1}^{\mathbf{k}} \exp \left\{ \frac{\mu_i}{4w} P_i^{\mathbf{k}} \right\} \right\} \right], \quad (3.8)$$

and systematically vary μ_i and evaluate $\Omega(\mu_i)$ until a step length close to the minimum of $\Omega(\mu_i)$ is found. This is done by successive parabolic fits and the determination of the respective minima. Two pieces of information needed for a parabolic fit are already available from the previous iteration and the calculation of the gradients $G_i^{\mathbf{k}}$, namely the value of Ω for $\mu_i = 0$ and its derivative $\left. \frac{\partial \Omega}{\partial \mu_i} \right|_{\mu_i=0} = \langle G_i; P_i \rangle / 4w$ which is given by the projection of the search direction onto the gradient. Note that β^{HS} and β^{PR} coincide in the case of an exact line search, namely, when $\Omega(\mu_i)$ is really minimized, since then the new gradient is perpendicular to the previous search direction and $\langle G_i; P_{i-1} \rangle = 0$.

3.5.2. Calculation of the spread and its gradient

A line search demands multiple evaluations of the spread Ω . Hence, its computation should be implemented in an efficient manner. We achieve this applying the symmetry relation from Eq. (3.3) in the following precalculated quantities:

$$a_n^{\mathbf{b}} = \frac{1}{N_{\mathbf{k}}} \sum_{\mathbf{k}} |M_{nn}^{\mathbf{k},\mathbf{b}}|^2 \quad (3.9)$$

$$A_n^{\mathbf{b}} = \frac{1}{N_{\mathbf{k}}} \sum_{\mathbf{k},m} \frac{1}{2} (|M_{nm}^{\mathbf{k},\mathbf{b}}|^2 + |M_{mn}^{\mathbf{k},\mathbf{b}}|^2) \quad (3.10)$$

$$l_n^{\mathbf{b}} = \frac{1}{N_{\mathbf{k}}} \sum_{\mathbf{k}} \text{Im}\{\ln M_{nn}^{\mathbf{k},\mathbf{b}}\} \quad (3.11)$$

$$L_n^{\mathbf{b}} = \frac{1}{N_{\mathbf{k}}} \sum_{\mathbf{k}} \text{Im}\{\ln M_{nn}^{\mathbf{k},\mathbf{b}}\}^2. \quad (3.12)$$

These quantities are used for evaluating the Wannier centers

$$\langle \mathbf{r} \rangle_n = 2 \sum_{\mathbf{b}^+} w_{\mathbf{b}} l_n^{\mathbf{b}} \mathbf{b} \quad (3.13)$$

and the parts of the spread functional (Eqs. (2.42)-(2.44))

$$\Omega_{\text{I}} = 2 \sum_{n=1}^J \sum_{\mathbf{b}^+} w_{\mathbf{b}} (1 - A_n^{\mathbf{b}}) \quad (3.14)$$

$$\Omega_{\text{OD}} = 2 \sum_{n=1}^J \sum_{\mathbf{b}^+} w_{\mathbf{b}} (A_n^{\mathbf{b}} - a_n^{\mathbf{b}}) \quad (3.15)$$

$$\Omega_{\text{D}} = \sum_{n=1}^J \left(2 \sum_{\mathbf{b}^+} w_{\mathbf{b}} L_n^{\mathbf{b}} - \langle \mathbf{r} \rangle_n^2 \right) \quad (3.16)$$

$$\Omega = \sum_{n=1}^J \left(2 \sum_{\mathbf{b}^+} w_{\mathbf{b}} (1 - a_n^{\mathbf{b}} + L_n^{\mathbf{b}}) - \langle \mathbf{r} \rangle_n^2 \right). \quad (3.17)$$

We further replace the expression for the gradient in Eq. (2.61) by

$$G_{mn}^{\mathbf{k}} = 4 \sum_{\mathbf{b}^+} w_{\mathbf{b}} \left(\mathcal{S}[\tilde{T}^{\mathbf{k},\mathbf{b}}]_{mn} - \mathcal{A}[\tilde{R}^{\mathbf{k},\mathbf{b}}]_{mn} \right), \quad (3.18)$$

with

$$\tilde{R}_{mn}^{\mathbf{k},\mathbf{b}} = M_{mn}^{\mathbf{k},\mathbf{b}} \overline{M_{nn}^{\mathbf{k},\mathbf{b}}} + \overline{M_{nm}^{\mathbf{k}-\mathbf{b},\mathbf{b}}} M_{nn}^{\mathbf{k}-\mathbf{b},\mathbf{b}} \quad (3.19)$$

and

$$\tilde{T}_{mn}^{\mathbf{k},\mathbf{b}} = \frac{M_{mn}^{\mathbf{k},\mathbf{b}}}{M_{nn}^{\mathbf{k},\mathbf{b}}} \left(\text{Im}\{\ln M_{nn}^{\mathbf{k},\mathbf{b}}\} + \mathbf{b} \cdot \langle \mathbf{r} \rangle_n \right) - \frac{\overline{M_{nm}^{\mathbf{k}-\mathbf{b},\mathbf{b}}}}{\overline{M_{nn}^{\mathbf{k}-\mathbf{b},\mathbf{b}}}} \left(\text{Im}\{\ln M_{nn}^{\mathbf{k}-\mathbf{b},\mathbf{b}}\} + \mathbf{b} \cdot \langle \mathbf{r} \rangle_n \right). \quad (3.20)$$

3.5.3. Convergence criteria

Marzari and coworkers [Mar+12] heuristically found that WFs are real valued up to a constant phase when they are maximally localized. This and a vanishing norm of the gradient $|G| = \sqrt{\langle G; G \rangle}$ provide two reliable checks whether the global minimum of the spread Ω is reached. With our implementation we are able to reach the global minimum for isolated subgroups of both occupied and unoccupied states while we cannot always reach it for wide band ranges ($J \sim 10 \dots 100$) of entangled bands. However, the theory outlined in sections 2.4 and 2.5 strictly holds for isolated groups of bands and does not necessarily guarantee that the gradient vanishes in the case of entangled bands. Nevertheless, the minimization algorithm significantly decreases Ω also in the case of entangled bands, and the resulting WFs are very useful for interpolations. Still, we do not call them maximally localized in the case $|G|$ remains finite. In order to determine whether the minimization procedure has converged we use two parameters, the real convergence cut-off $\delta > 0$ and a positive integer I . In the vicinity of a potential minimum different behavior can occur depending on the actual method used. In the case of an isolated group of bands, where the theory strictly holds, $|G|$ will tend to zero and the algorithm is aborted when $|G|$ becomes smaller than the cut-off δ . However, when we use a fixed step length instead of a line search it may happen that the procedure hops around the exact minimum but never reaches it when the step length becomes too large in the vicinity of the minimum. Then Ω starts to oscillate, and a linear function is fitted to the last I values of Ω . We stop searching when the slope of the linear fit becomes smaller than the cut-off δ . Moreover, in the case of a fixed step length, Ω does not necessarily decrease in each iteration while still being decreasing over several iterations. For this reason, we find it impractical to use differences of Ω between two consecutive iterations as a convergence criterion. In the case of entangled bands we are not always able to approach $|G| = 0$ with arbitrary precision. In that case, usually the second convergence criterion is applied. In the following section we will further describe the behavior of the minimization algorithm.

3.5.4. Starting point dependence and convergence

In this section, we analyze the convergence behavior of the minimization algorithm for the spread Ω as outlined in Sec. 2.5.3 or more detailed in Ref. [MV97]. First, we check whether the algorithm arrives at the global minimum of the spread functional and how much it depends on the starting point. Then, we compare the different CG methods described in Sec. 3.5.1 among each other and with the steepest descent approach. In the end, the convergence w.r.t. the sampling density of the BZ is investigated for the spread Ω and the interpolation accuracy.

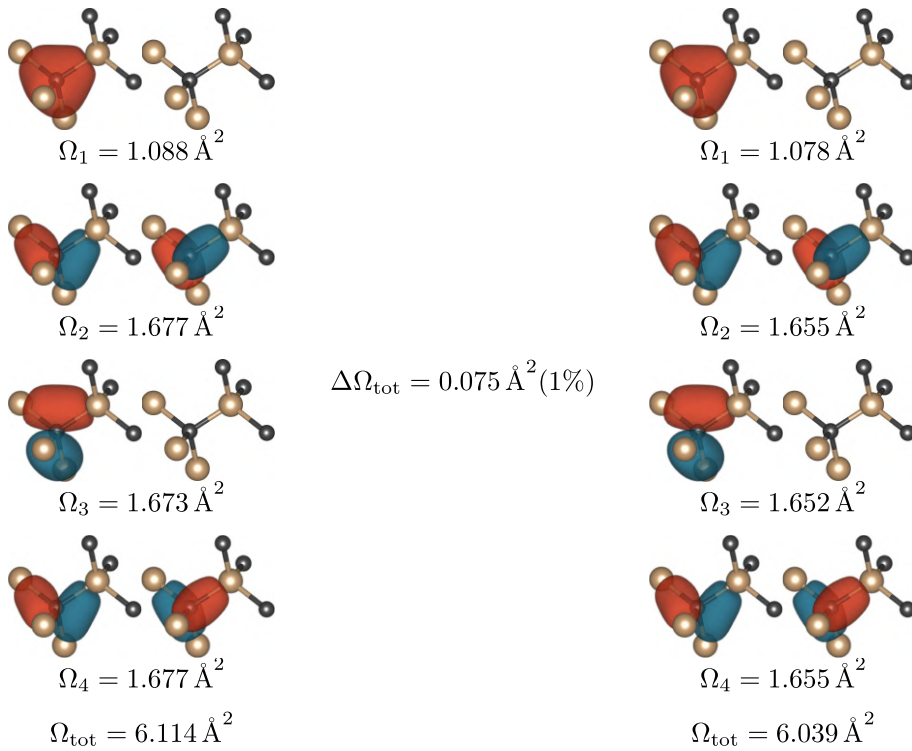


Fig. 3.3: Local minimum for SiC reached from simple projection

WFs from simple projection on carbon s - and p -orbitals before the minimization (left panel) and after the minimization (right panel). The minimization algorithm gives a reduction of Ω_{tot} by 0.075 \AA^2 (about 1%) and changes the input functions just very slightly. Real part (left) and imaginary part (right) are shown in each panel.

In the discussion of the starting-point dependence we remain at the example of the four valence bands in silicon carbide introduced in Sec. 3.3. We minimize the spread Ω starting from two different starting points. In the first case, we start with WFs obtained via simple projection on one s - and three p -orbitals located at the carbon atom (left panel in Fig. 3.2). The result is depicted in Fig. 3.3. The four WFs obtained by projection are

centered at the same atom as the projection functions and clearly reflect their distinct s - and p -character. The minimization algorithm varies them just slightly and converges at almost the same functions after a reduction of Ω of about 1%. The norm of the gradient of the spread Ω is in the order of 10^{-7} after convergence, that means the functions shown on the right in Fig. 3.3 really represent a local minimum.

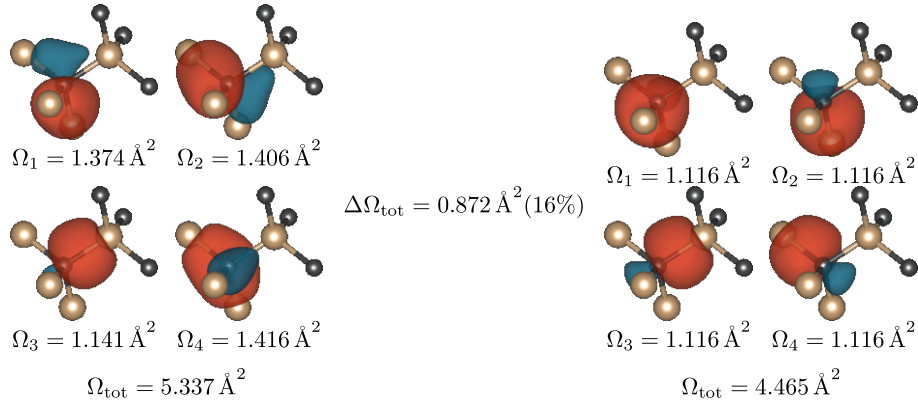


Fig. 3.4: Global minimum for SiC reached from OPF

On the left-hand side four WFs corresponding to the four valence bands in silicon-carbide are depicted. They are generated using OPFs built out of 61 local orbitals with angular character up to $l = 2$. They better describe the shape of the MLWFs (right-hand side) compared to the WFs obtained from simple projection. Thus, OPFs enable the minimization procedure to reach the global minimum of the spread Ω .

In the second case, we start from WFs that are obtained from projection on OPFs. The OPFs have constructed using 61 local orbitals with spherical harmonics up to $l = 2$ centered on both the carbon (39 orbitals) and the silicon atom (22 orbitals). The result is shown in Fig. 3.4. The functions obtained in such a manner are already almost real valued (the imaginary part is about two orders of magnitude smaller than the real part) which is why in Fig. 3.4 just the real part is given. The initial WFs ($\Omega = 5.337 \text{ \AA}^2$) are already more localized than in the case of the simple projection ($\Omega = 6.114 \text{ \AA}^2$) and show a very different and asymmetric shape. This shape is in better agreement with the real MLWFs. In this case, the minimization procedure is able to reach the global minimum of the spread after a reduction of Ω by 16%. The resulting MLWFs are depicted on the right-hand side of Fig. 3.4. They form a set of four symmetrically equivalent sp^3 -like orbitals centered on the four tetrahedral Si-C bonds. This reveals the reason for the failure of the minimization in the first case. Using local orbitals that are centered on atom sites and zero on the bond centers do not provide a suitable guess for WFs that are bond-centered.

Therefore we assume that functions that are still localized but not necessarily restricted to the MTs and not necessarily atom-centered will be more practical to provide a good starting point for the minimization and also for the generation of OPFs.

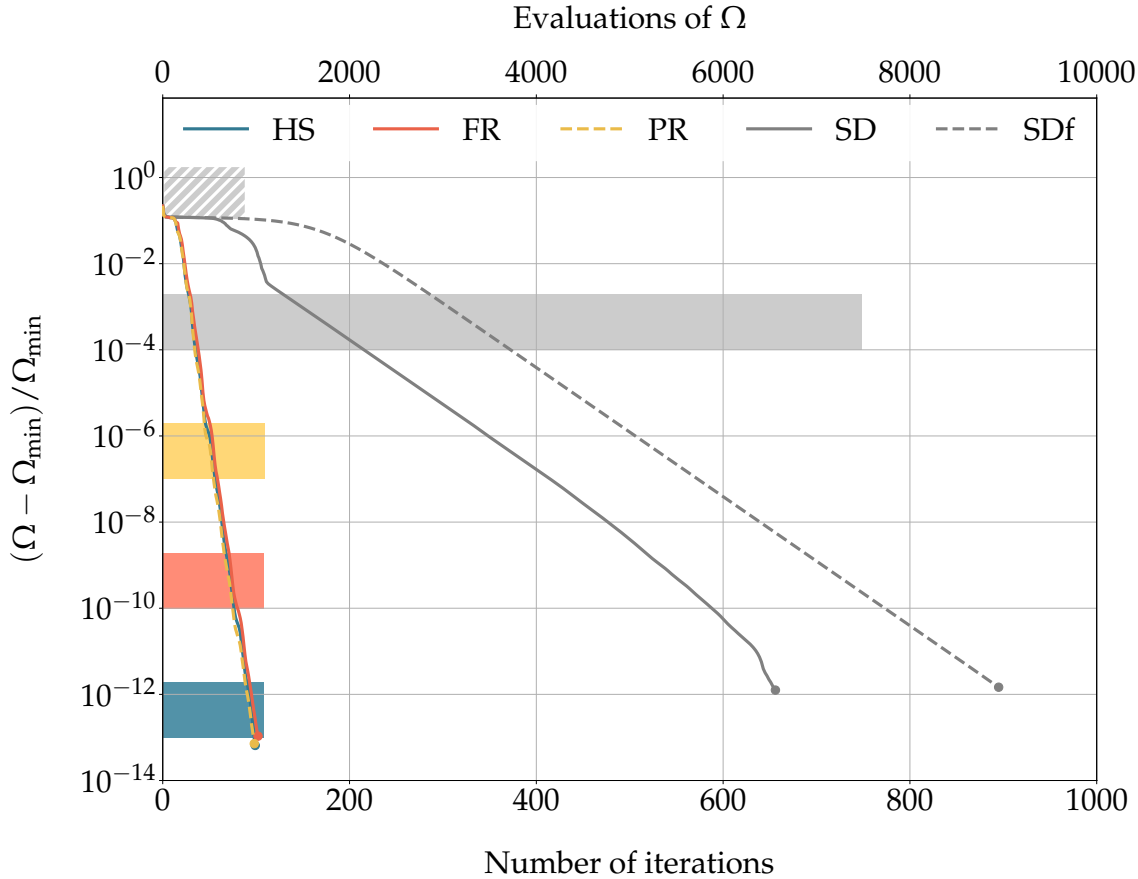


Fig. 3.5: Convergence of different minimization methods

Minimization of the spread Ω starting from WFs obtained from OPFs using different minimization algorithms. The CG algorithms with line search (colored lines) converge considerably faster than the steepest descent (SD) algorithms (gray lines). However, a properly chosen fixed step length (SDf) is able to compete with the line search algorithm in some cases since it requires much less evaluations of the spread (bars).

Now, we show how the different minimization methods arrive at the global minimum starting from the functions on the left in Fig. 3.4. We consider the algorithm to be converged when the norm of the gradient $|G|$ drops below 10^{-6} for all methods. The CG methods and the steepest descent (SD) algorithm are performed with a line search. Additionally we carry out the steepest descent approach with a fixed step length (SDf) that was chosen to be the maximum step length that leads to convergence. As expected,

the three CG methods converge much faster compared to the SD approach. In our test case, convergence is achieved after 98, 99, and 102 iterations for the PR, the HS, and the FR update parameter, respectively. Fig. 3.5 shows that there is just a slight difference in the behavior of the HS and PR methods which indicates that the line search is almost exact as explained in Sec. 3.5.1. But also the performance of the FR update does not differ much from the other two CG algorithms in this case. For a comparison, the SD minimizations converged after 656 iterations with line search and 895 iterations with a suitable chosen fixed step length. On one hand this manifests the superiority of the CG algorithms over the SD approach but, on the other hand, we also see that a minimization with a suitably chosen fixed step length can be competitive in some cases, especially since it requires much fewer evaluations of the spread Ω (one evaluation/iteration with fixed step length vs. ~ 10 evaluations/iteration with line-search). The latter fact deserves attention since in the current implementation, the time needed for the multiple evaluations of the spread Ω that are needed in order to determine the optimal step length is not negligible, and an algorithm with fixed step length might converge faster in terms of computational time compared to an algorithm with optimal determined step lengths although the latter one requires fewer iterations. Therefore, the minimization procedure of choice could be a CG combined with a fixed step length or an inexact faster line search. Also hybrid approaches with a frequently adjusted temporarily fixed step lengths are possible. However, this will need further investigations.

We conclude this section by discussing the convergence with respect to the \mathbf{k} -point density of the supporting grid. Therefore, we calculate the MLWFs corresponding to the valence bands of diamond on cubic \mathbf{k} -meshes $n_k \times n_k \times n_k$ with n_k ranging from 2 to 10. In order to determine the density of \mathbf{k} -points needed to generate MLWFs that are suitable for further interpolations with a desired accuracy we calculated again the root mean square of the differences between calculated and interpolated energies, $\delta\varepsilon_{\text{RMS}}$, as explained above. Figure 3.6 shows that the interpolation error drops exponentially with the number of \mathbf{k} -points in the supporting grid. This is an effect of the exponential localization property of WFs. A finer sampling of the BZ corresponds to a larger SC on which the WFs are periodic. As a consequence, the overlap of a WF with its images in neighboring SCs (which causes the error in the interpolation) also drops exponentially with increased SC size. We find for this case that approximately three \mathbf{k} -points per \AA^{-1} in each direction in reciprocal-space (in the following referred to as *one-dimensional* (1D) \mathbf{k} -point density),

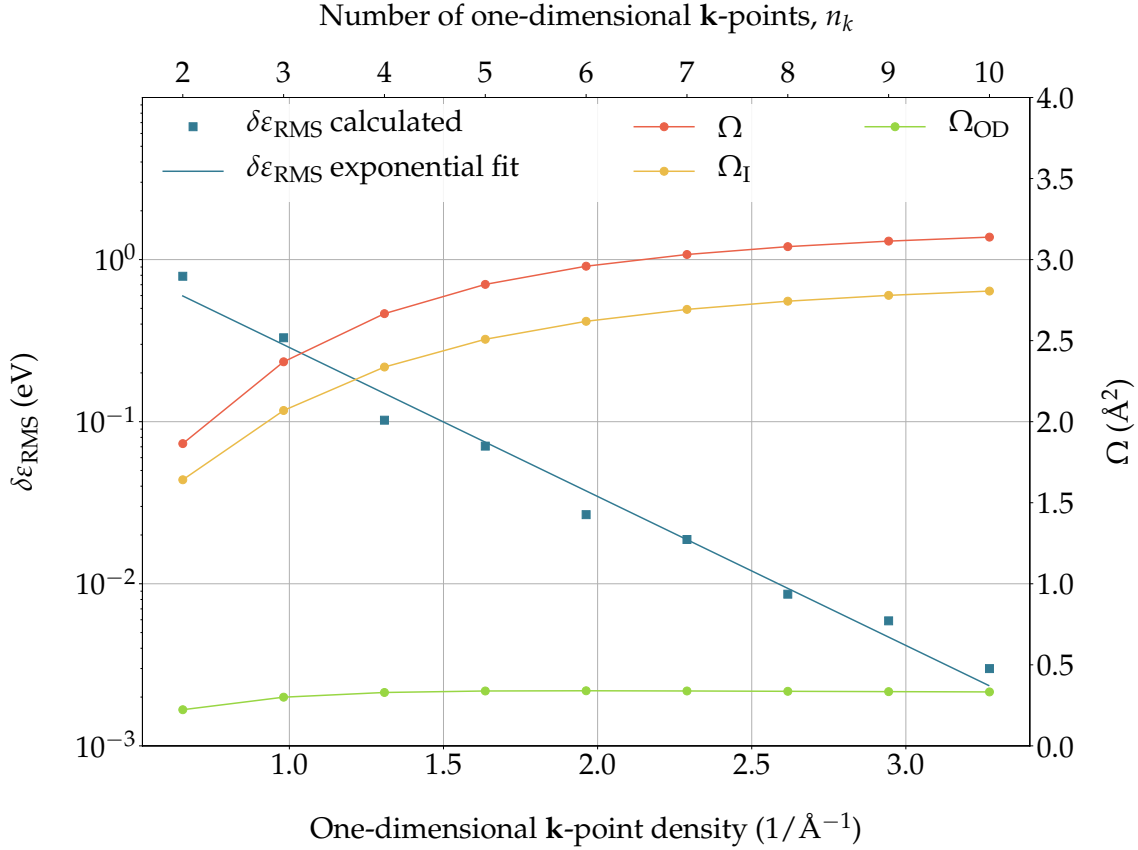


Fig. 3.6: k-point convergence of the prediction error and the spread Ω

The error in the prediction of electron energies $\delta\epsilon_{\text{RMS}}$ (blue squares, left axis) drops exponentially with increasing \mathbf{k} -point density. Predictions up to 10 meV require about 3 \mathbf{k} -points per \AA^{-1} in each direction of the reciprocal-space. The spread Ω (colored circles, right axis) converges slowly w.r.t. the \mathbf{k} -point density due to the slow convergence of Ω_I . The lines serve to guide the eye.

corresponding to $n_k = 8$, are sufficient to interpolate the eigenenergies within 10 meV on average. These results are in good agreement with the numbers presented by Yates and coworkers [Yat+07]. Additionally, Fig. 3.6 illustrates that the actual spread Ω converges slowly with respect to \mathbf{k} -points and is not even converged for $n_k = 10$. A splitting of Ω in its different contributions shows that it is the gauge independent part Ω_I that converges badly while the off-diagonal part Ω_{OD} is already converged for $n_k = 6$. The diagonal part Ω_{D} is zero in this case due to the inversion symmetry of the diamond crystal. The increase in Ω_I and its bad convergence behavior is in good agreement with the considerations for silicon made in Ref. [MV97].

3.6. Interpolation

3.6.1. Choice of the lattice vector set \mathbf{R}

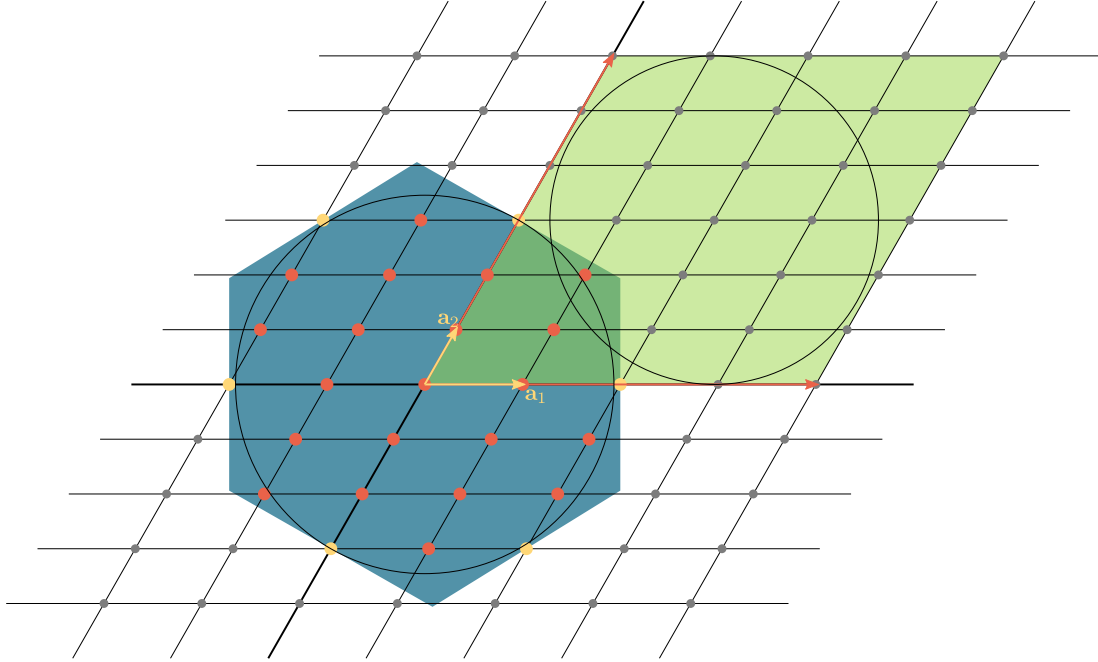


Fig. 3.7: Real-space lattice vectors on Wigner-Seitz super cell

The red and yellow circles illustrate the lattice vectors \mathbf{R} that are used in the calculation of Fourier sums. They are included in a Wigner-Seitz cell of the SC conjugate to the BZ sampling (green shaded area). The phases for equivalent lattice vectors (yellow circles) are averaged.

Up to this point, when generating $U^{\mathbf{k}}$, we have just considered WFs centered in the home unit cell at $\mathbf{R} = 0$ in the calculation of the spread Ω . In order to use WFs for interpolations, sums over real-space lattice vectors \mathbf{R} such as in Eqs. (2.28) or (2.29) have to be computed. Instantly the question arises which real-space lattice vectors \mathbf{R} to choose. The \mathbf{R} -vectors need to form a SC containing $N_{\mathbf{k}}$ unit cells. However, there is no unique and obvious way to choose them. Although their choice does not effect the construction of the transformation matrices $U^{\mathbf{k}}$, we find that the quality of the interpolation may strongly depend on it. This was also reported in the literature previously (e.g. in Ref. [Yat+07]). In this implementation, we select the set of vectors \mathbf{R} to form the Wigner–Seitz cell (blue area in Fig. 3.7) of the $n_{k_1}\mathbf{a}_1 \times n_{k_2}\mathbf{a}_2 \times n_{k_3}\mathbf{a}_3$ real-space SC (green area), where $n_{k_1}, n_{k_2}, n_{k_3}$ describe the sampling of the BZ and $N_{\mathbf{k}} = n_{k_1}n_{k_2}n_{k_3}$ is the total number of \mathbf{k} -points. We

center this SC at the origin and perform an additional averaging of the phases $e^{\pm i\mathbf{k}\cdot\mathbf{R}}$ for equivalent points (with the same distance from the origin) on the Wigner-Seitz cell boundary (yellow circles). In the example illustrated in Fig. 3.7, two opposite points on the boundary are pairwise equivalent. The main idea behind this approach is to find a SC that encloses a possibly large sphere in order to maximize the distance, and thus the overlap between a WF and its periodic images in the neighboring SCs. However, this method, in general, does not give the optimal SC. A method that searches for all possible SCs that include $N_{\mathbf{k}}$ unit cells and finds the one which encloses the largest sphere among them was provided by Hart and Forcade [HF08] but is not yet implemented in this work.

3.6.2. Interpolation of band-characters

Chemical interpretation of bands obtained in a DFT calculation requires to decompose them in particular atomic states. We use the Wannier interpolation to do so. We start the analysis by calculating the contribution of a single MT α to the partial density $\rho_{n,\mathbf{k}}$ at a given \mathbf{k} -point in the BZ. The wavefunction inside this MT is expanded into spherical harmonics

$$\Psi_{n,\mathbf{k}}^{\alpha}(\mathbf{r}_{\alpha}) = \sum_l \sum_{m=-l}^l \varphi_{n,\mathbf{k},lm}^{\alpha}(r_{\alpha}) Y_{lm}(\hat{\mathbf{r}}_{\alpha}), \quad (3.21)$$

with the radial expansion functions $\varphi_{n,\mathbf{k},lm}^{\alpha}$. The partial density integrated over the MT α reads

$$\begin{aligned} \int_{\text{MT}_{\alpha}} d\mathbf{r} \rho_{n,\mathbf{k}}^{\alpha}(\mathbf{r}) &= \int_{\text{MT}_{\alpha}} d\mathbf{r} |\Psi_{n,\mathbf{k}}^{\alpha}(\mathbf{r})|^2 \\ &= \sum_l \sum_{m=-l}^l \int_0^{R_{\alpha}} r^2 |\varphi_{n,\mathbf{k},lm}^{\alpha}(r)|^2 dr \\ &= \sum_l b_{n,\mathbf{k}}^{\alpha,l}. \end{aligned} \quad (3.22)$$

We interpret the l -resolved quantity $b_{n,\mathbf{k}}^{\alpha,l}$ as the contribution of electrons with angular character l and wavevector \mathbf{k} inside the MT α to the energy band n . Further, we expand the radial functions $\varphi_{n,\mathbf{k},lm}^\alpha$ in our (L)APW+lo basis

$$\begin{aligned}\varphi_{n,\mathbf{k},lm}^\alpha(r_\alpha) &= \sum_{\mathbf{G}+\mathbf{k}} C_{n,\mathbf{G}}^{\mathbf{k}} \sum_{o=1}^{M_l^\alpha} A_{n,lm,o,\mathbf{G}+\mathbf{k}}^\alpha u_{l,o}^\alpha(r_\alpha) + \sum_{\mathbf{L}} C_{n,\mathbf{L}}^{\mathbf{k}} f_{l,\mathbf{L}}^\alpha(r_\alpha) \delta_{\alpha\alpha_{\mathbf{L}}} \delta_{ll_{\mathbf{L}}} \delta_{mm_{\mathbf{L}}} \\ &= \sum_{\lambda} B_{n,\lambda,lm}^{\mathbf{k},\alpha} g_{\lambda,l}^\alpha(r_\alpha),\end{aligned}\quad (3.23)$$

where the second line is introduced for the sake of simplification. The index λ is either the (L)APW matching order o or the index of a local orbital \mathbf{L} . The coefficients $B_{n,\lambda,lm}^{\mathbf{k},\alpha}$ are either the matching coefficients contracted with the eigenvectors or the eigenvectors for the local-orbitals combined with the deltas. The function $g_{\lambda,l}^\alpha$ is either an (L)APW or a local orbital radial function. Now we are able to express $b_{n,\mathbf{k}}^{\alpha,l}$ in terms of the coefficients $B_{n,\lambda,lm}^{\mathbf{k},\alpha}$ and radial overlap integrals $I_{\lambda\lambda'}^{\alpha,l}$

$$\begin{aligned}b_{n,\mathbf{k}}^{\alpha,l} &= \sum_{m=-l}^l \sum_{\lambda,\lambda'} B_{n,\lambda,lm}^{\mathbf{k},\alpha} \overline{B_{n,\lambda',lm}^{\mathbf{k},\alpha}} \int_0^{R_\alpha} r^2 g_{\lambda,l}^\alpha(r) g_{\lambda',l}^\alpha(r) \\ &= \sum_{m=-l}^l \sum_{\lambda,\lambda'} B_{n,\lambda,lm}^{\mathbf{k},\alpha} I_{\lambda\lambda'}^{\alpha,l} \overline{B_{n,\lambda',lm}^{\mathbf{k},\alpha}}.\end{aligned}\quad (3.24)$$

This formulation has the advantage that the radial integrals are \mathbf{k} -point independent and just need to be calculated once. Then, the problem is reduced to linear algebra operations. When we now want to calculate $b_{n,\mathbf{q}}^{\alpha,l}$ for an arbitrary wavevector \mathbf{q} we just need to know the coefficients $B_{n,\lambda,lm}^{\mathbf{q},\alpha}$ at this point. Therefore we apply the expression for the Wannier interpolated wavefunction (2.70) and yield

$$\varphi_{n,\mathbf{q},lm}^\alpha(r_\alpha) = \sum_{\lambda} \sum_{\mu} V_{\mu n}^{\mathbf{q}} \sum_{\mathbf{R}} e^{i\mathbf{q}\cdot\mathbf{R}} \frac{1}{N_{\mathbf{k}}} \sum_{\mathbf{k}} e^{-i\mathbf{k}\cdot\mathbf{R}} \sum_{\nu} U_{\nu\mu}^{\mathbf{k}} B_{\nu,\lambda,lm}^{\mathbf{k},\alpha} g_{\lambda,l}^\alpha(r_\alpha). \quad (3.25)$$

This lengthy expression is simplified in two steps. First, we perform the Fourier sum over \mathbf{k} which corresponds to a transformation of the $B^{\mathbf{k},\alpha}$ to real-space

$$\varphi_{n,\mathbf{q},lm}^\alpha(r_\alpha) = \sum_{\lambda} \sum_{\mu} V_{\mu n}^{\mathbf{q}} \sum_{\mathbf{R}} e^{i\mathbf{q}\cdot\mathbf{R}} B_{\mu,\lambda,lm}^{\mathbf{R},\alpha} g_{\lambda,l}^\alpha(r_\alpha). \quad (3.26)$$

Once the coefficients $B^{\mathbf{R},\alpha}$ are computed and stored they are transformed back to the desired point \mathbf{q} in reciprocal-space using the inverse Fourier sum

$$\varphi_{n,\mathbf{q},lm}^{\alpha}(r_{\alpha}) = \sum_{\lambda} B_{n,\lambda,lm}^{\mathbf{q},\alpha} g_{\lambda,l}^{\alpha}(r_{\alpha}) . \quad (3.27)$$

Now all ingredients are provided to compute the interpolated band-character $b_{n,\mathbf{q}}^{\alpha,l}$.

4. Applications

In the following sections we present the application of MLWFs to different groups of materials. We start with closely packed systems with small unit cells such as diamond and other diamond-like compounds with two atoms per unit cell and proceed to more complex titanium dioxide with six atoms per unit cell and a hybrid organic–inorganic compound with 43 atoms. We further present the applicability of MLWFs to interpolations in metals. The discussion is focused on the interpolation of band-structures obtained from different levels of theory. We show Wannier interpolated band-structures built from simple KS eigenstates obtained using local or semi-local xc-functionals, proceeding to non-local hybrid xc-functionals and eventually arriving at eigenenergies that were computed using many-body perturbation-theory within the G_0W_0 approach.

4.1. Diamond-like structures

4.1.1. Band-structure interpolation

When interpolating KS band-structures we have the possibility to evaluate the quality of the results by comparison with the actual eigenenergies that were calculated solving the secular equations at each point along the BZ path from a density that has been obtained within a fully self-consistent calculation. In contrast to LDA and GGA where the KS-potential is (semi)local, hybrid functionals, such as the PBE0 potential, involve also a Fock exchange that is non-local both in real and reciprocal-space. A calculation of the Hamiltonian matrix at arbitrary \mathbf{k} -points \mathbf{q} requires the knowledge of the wavefunctions at $\mathbf{q} - \mathbf{k}$ which are usually not known. Therefore, a direct calculation of band-structures within this framework is usually avoided due to the considerable computational cost. Instead, interpolation schemes are applied to obtain the energies along the desired BZ-path. One natural approach to the energy dispersion is using a Fourier interpolation (e.g. as proposed by Pickett, Krakauer, and Allen [PKA88]), i.e., interpolating the energies given on the three-dimensional grid in reciprocal-space using sinusoidal functions. This method is currently used within the `exciting` code. Now, we are going to compare both interpolation schemes, the purely mathematical Fourier interpolation and the physically motivated Wannier interpolation.

Therefore, we consider diamond calculated using the PBE0 xc-functional, i.e. 25% of exact exchange from Hartree–Fock. The eigenenergies obtained on a $8 \times 8 \times 8$ \mathbf{k} -grid are

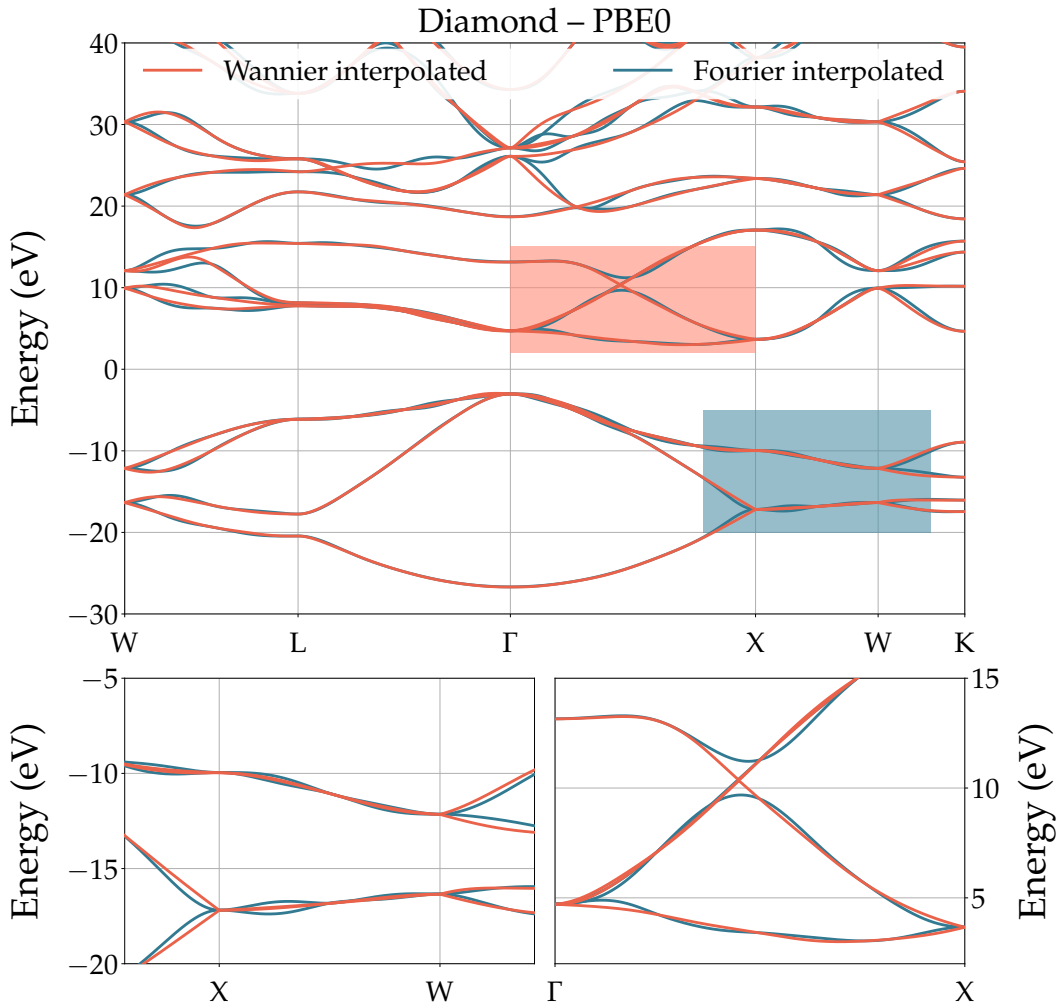


Fig. 4.1: Fourier and Wannier interpolated band-structure for diamond

The band-structure of diamond based on a DFT calculation using the non-local hybrid xc-functional PBE0 is depicted. It was obtained using the mathematical Fourier interpolation scheme (blue) or the physically grounded Wannier interpolation (red). The Fourier interpolation fails to properly reproduce neuralgic physical features such as band-degeneracies, band-crossings and band-splittings.

interpolated in order to obtain the band-dispersion along the path connecting different high-symmetry points in the BZ. In Fig. 4.1, we present the band-structure obtained using either the Fourier (blue lines) or the Wannier (red lines) scheme. It is evident that the Fourier interpolation gives qualitatively wrong band-dispersions in certain areas of the band-structure while the Wannier interpolation does not show this behavior. The Fourier interpolation fails to reproduce several neuralgic features. The consideration of degenerate energy bands reveals that, in contrast to the Wannier interpolation, the Fourier interpo-

lation is not capable to reproduce this degeneracy and gives an unphysical splitting of the bands. In the present example, this is the case for the valence bands along the X-W direction which are pairwise degenerate (blue shaded area in Fig. 4.1, magnified in the lower left panel). Furthermore, it fails to recover some band-splittings, e.g. as they occur in the lower valence bands at the X point (lower left panel in Fig. 4.1). Here, the smoothness of this mathematical interpolation scheme is rather a hindrance than an advantage. This is also the case in the vicinity of band-crossings where the crossing point is not part of the supporting grid, as it occurs in lower group of conduction bands along the Γ -X direction (red shaded area in Fig. 4.1, magnified in the lower right panel). Here, the Wannier interpolation perfectly reproduces the physically correct crossing while the Fourier interpolation suggests no crossing at all. This shortcoming can probably be overcome by rearranging the underlying input energies such that they are grouped according to their belonging to a 'physical' band rather than ordering them numerically with increasing energy. However, this requires distinct knowledge about the nature and origin of the energy bands and becomes more and more difficult in the vicinity of points where many bands are close to or crossing each other (e.g. at the upper most part of the depicted band-structure at the Γ point). We see that, even for this relatively densely sampled BZ with 8^3 \mathbf{k} -points, the Fourier interpolations fails to produce a qualitatively correct band-structure for a prototypical material like diamond. This purely mathematical scheme typically fails in the vicinity of physically neuralgic points such as band-degeneracies, band-crossings or band-splittings. The physically grounded Wannier interpolation, however, gives almost exact results and is capable of reproducing such important physical features.

4.1.2. Chemical bonding analysis

Localized molecular orbitals are widely used in chemistry in order to analyze the character of chemical bonding. Hence, it appears natural to expand this analysis to localized orbitals in solids, such as MLWFs. Since MLWFs are uniquely defined in insulating and semiconducting systems they provide a useful tool to investigate hybridization and polarity of bonds ([Mar+12]). Abu-Farsakh and Qteish [AQ07] even suggested a bond-ionicity scale based on MLWFs. Within this work, we have computed the four symmetrically equivalent MLWFs corresponding to the four valence bands of different group IV and III-V semiconductors in the zincblende structure (Fig. 4.2). They all are formed by two sp^3 -hybridized orbitals centered on two atoms forming a bond. Some of them are fully or

almost symmetric w.r.t. a plane perpendicular to the bond-axis while others exhibit clear asymmetries. In order to approach these differences systematically, the compounds are ordered according to the difference in the electronegativity χ of the involved elements.

The WFs of the purely covalent Si-Si and C-C bonds in silicon and diamond, respectively, are fully symmetric. Also for boron phosphide, the WFs are almost symmetric. This is in accordance with the small difference in χ ($\Delta\chi = 0.15$). In contrast, aluminum phosphide and silicon carbide possess strongly asymmetric WFs according to their larger differences in the electronegativity ($\Delta\chi = 0.58$ and $\Delta\chi = 0.65$, respectively). However, there are examples that do not follow this trend. Cubic boron nitride, for example, shows the greatest difference in χ , $\Delta\chi = 1.00$, but its WFs are less asymmetric than those of SiC or AlP.

Up to this point, the discussion was rather qualitative and the question remains how to visually compare different WFs. In the left column of Fig. 4.2, the orbitals are drawn according to a common iso-value. Another possibility is depicted in the right column. Here, the iso-value was chosen differently for each material such that the bond centered bulbs (red indicate positive values) have the same size w.r.t. to the corresponding crystal structure. Both choices may lead to slightly different interpretations. A more quantitative measure can be provided by the visualizations of surfaces that include a certain fraction of the integral of the complete WF. That means that the iso-value λ has to be chosen such that the integral

$$\int_{\mathbb{R}^3} d\mathbf{r} |w_{n,\mathbf{R}}(\mathbf{r})|^2 \theta_\lambda(\mathbf{r}) = \alpha, \quad (4.1)$$

where $\theta_\lambda(\mathbf{r}) = 0$ if $|w_{n,\mathbf{R}}(\mathbf{r})|^2 < \lambda$ and 1 otherwise. $\alpha \in (0, 1]$ is a fraction of total integral. Another way to quantify the above phenomenological descriptions is provided by the use of the centers of the WFs $\langle \mathbf{r} \rangle_n$. Therefore, we introduce the parameter σ that measures the offset of the Wannier center from the bond center. That means, $\sigma = 0$ when the WF is centered right in the middle of the bond and $\sigma = 1$ when the Wannier center coincides with one of the atom positions. In Fig. 4.2, the centers of the WFs are indicated with a white sphere. This measure verifies the former qualitative impression. As it clearly correlates with the difference in the electronegativity, it provides a good measure for the polarity of the bond. It has to be mentioned that different localization criteria may result in differently MLWFs. However, the presented characteristics like shape or position of

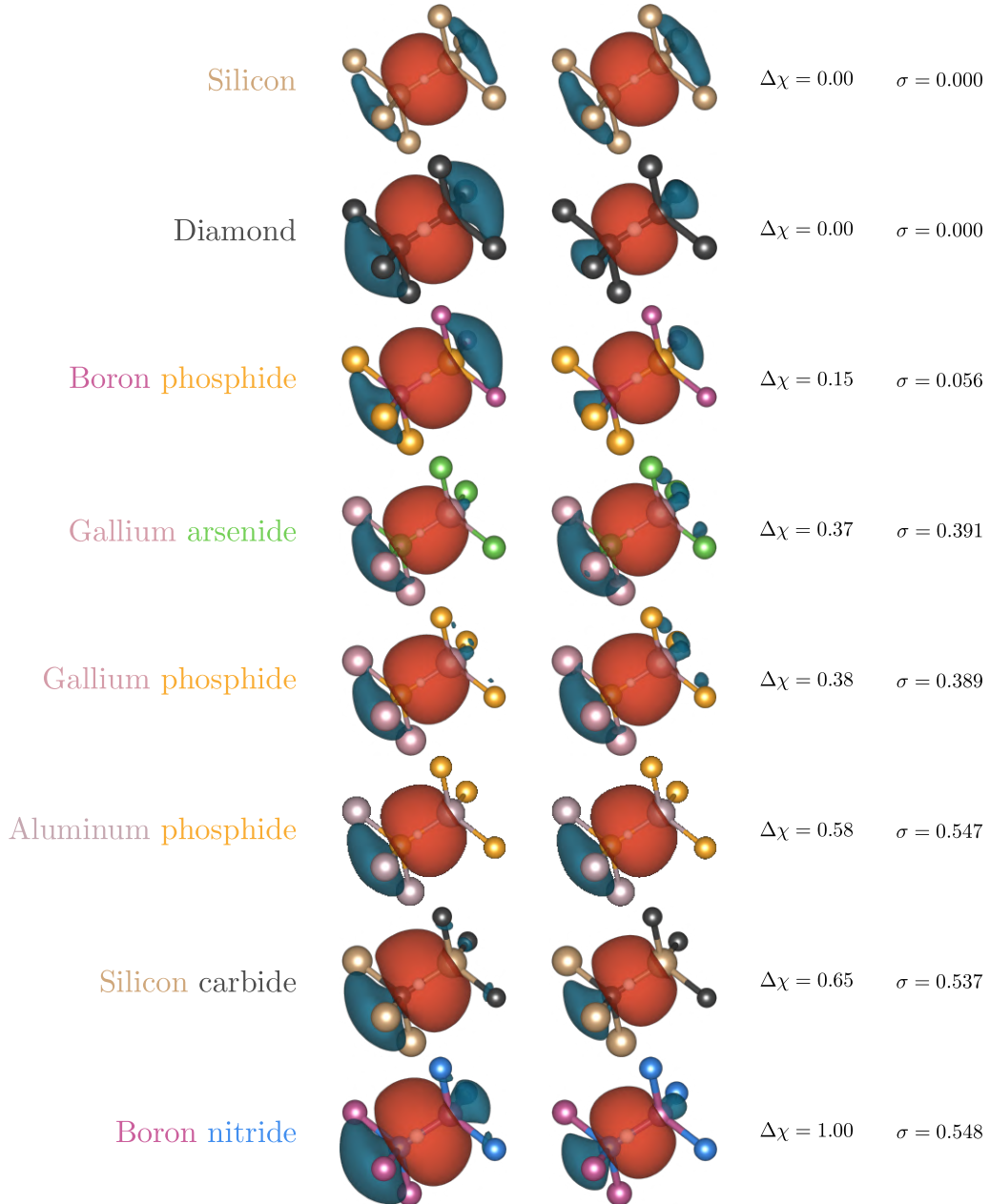


Fig. 4.2: MLWFs in group IV and III-V semiconductors

For each material, one of the four equivalent real valued sp^3 -like MLWFs corresponding to the four valence bands is illustrated. The compounds are ordered from top to bottom with increasing difference in the electronegativity $\Delta\chi$ of the involved elements. In the left column they are shown for the same iso value while in the right column the iso value was chosen differently such that the bond-centered (red) bulbs are of equal size w.r.t. the according crystal structure. The white spheres indicate the positions of the Wannier centers and σ measures its displacement from the bond center.

the Wannier centers are reported to be often independent of the method or criterion used to generate localized WFs [Mar+12].

4.2. Titanium dioxide

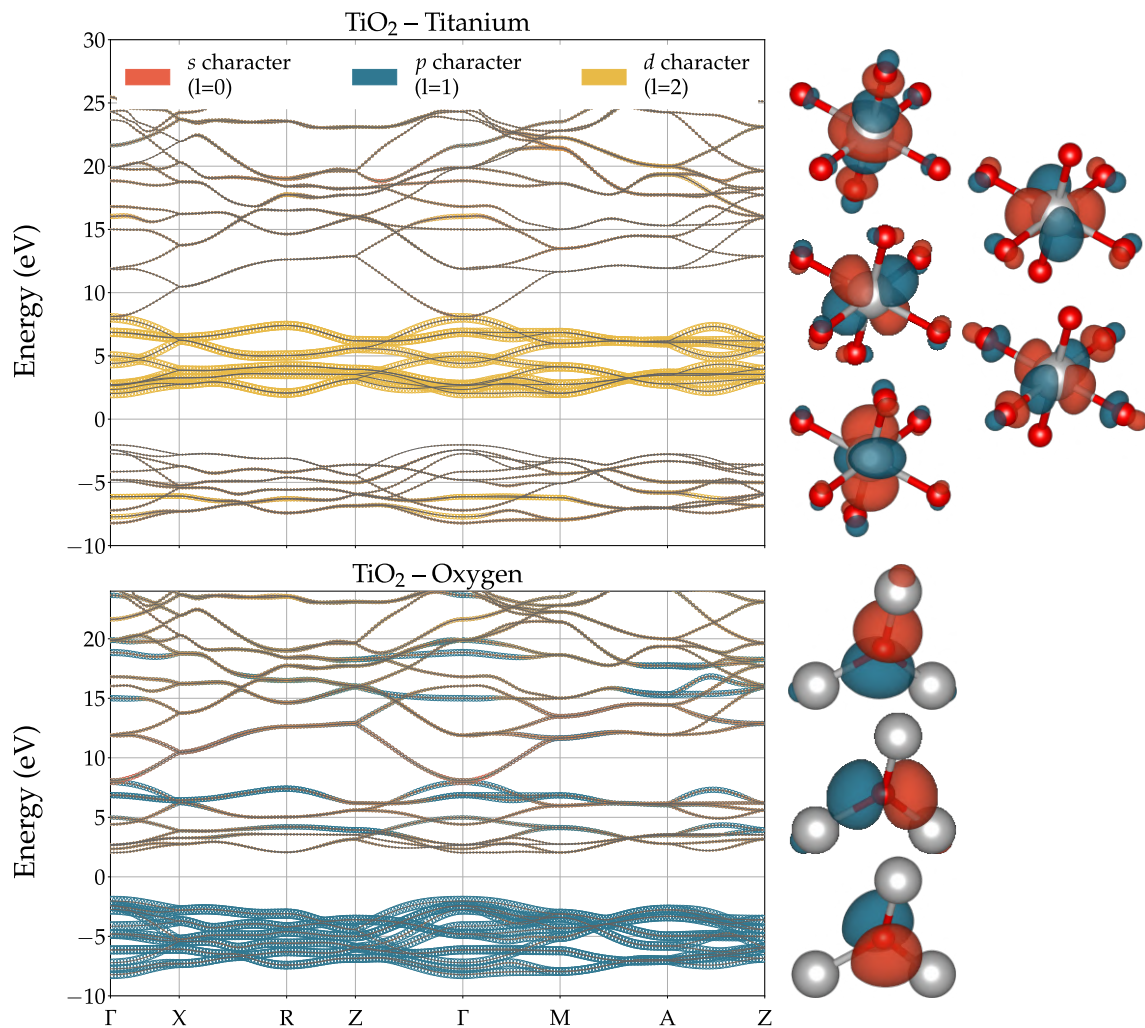


Fig. 4.3: Interpolated band-structure of TiO_2 indicating the atomic character

The band-structure was obtained using Wannier interpolation on top of a DFT calculation using the PBE0 functional. The colored circles display the l -resolved contribution of electrons from titanium (top) and oxygen (bottom) to the different energy bands. On the right, the MLWFs corresponding to the twelve valence bands (bottom) and the first ten conduction bands (top) are illustrated.

In this section, we extend the demonstration of band-structures for hybrid xc-potentials as introduced in Sec. 4.1.1 to a more complex compound, namely TiO_2 in the rutile

structure. In addition, we present the calculation of band-characters by the use WFs and show how it reflects in MLWFs corresponding to isolated subgroups of bands. In Fig. 4.3, the Wannier interpolated band-structure of TiO_2 , obtained from a DFT calculation using the hybrid functional PBE0, is depicted. The BZ was sampled with $4 \times 4 \times 6$ points which corresponds to a 1D \mathbf{k} -point density of about $2.8 \mathbf{k}\text{-points}/\text{\AA}^{-1}$. The illustrated energy range contains two isolated groups of bands. One is formed by the twelve valence bands and the other is formed by the ten lowest unoccupied bands. An investigation of the band-character (colored circles), that means $b_{n,\mathbf{k}}^{\alpha,l}$ as defined in Eq. (3.21), shows that these two subgroups can be clearly assigned to a specific species. The band-character for $l = 0, 1, 2$ is summed over all contributions from titanium atoms (silver atoms, top panel) and oxygen atoms (red atoms, bottom panel). The character-plot reveals that the twelve valence bands originate mainly from oxygen p -like electrons (blue circles, bottom panel) while the group of the first ten conduction bands show mainly titanium d -like character (yellow circles, top panel). This observation can be confirmed by the examination of the MLWFs corresponding to this two isolated groups of bands. The twelve valence bands correspond to three almost purely p -like WFs centered on oxygen atoms (three for each of the four oxygen atoms in the unit cell). Accordingly, the ten lowest conduction bands are represented by five dominantly d -like WFs centered on titanium atoms (five for each of the two titanium atoms in the unit cell). However, the WFs on the top also reflect a small contribution from of oxygen p orbitals, as visible in the conduction bands in the lower band-structure plot.

4.3. Hybrid organic–inorganic system

In this section, we simultaneously demonstrate the ability to generate strongly localized WFs for a complex hybrid organic–inorganic system and their usage for the calculation of quasi-particle band-structures. The system under consideration consists of pyridine molecules adsorbed on the $(10\bar{1}0)$ surface of a wurtzite ZnO slab and is made up of 43 atoms in the unit cell. For similar reasons as for non-local xc-functionals, namely the complexity of the calculation of the non-local \mathbf{k} -dependent self-energy Σ and the corresponding correction to the KS eigenvalues $\epsilon_n^{\mathbf{k}}$, quasi-particle energies at arbitrary \mathbf{k} -points are not directly accessible within the one-shot GW approximation and energy interpolation is required. In the framework of the one-shot GW method (also referred to as G_0W_0 approximation) the KS-wavefunctions are used to determine the Green’s function

and the self-energy while themselves remain unchanged. Therefore the construction of the transformation matrices $U^{\mathbf{k}}$ is perfectly equivalent to the DFT case. The only difference in the interpolation procedure in comparison to the DFT case is the replacement of the KS energies $\epsilon_n^{\mathbf{k}}$ by the quasi-particle energies $\epsilon_n^{\text{QP},\mathbf{k}}$ in the eigensystem interpolation outlined in Sec. 2.6.2. As already done in Sec. 4.1.1, we compare the band-structures obtained using the Fourier and the Wannier interpolation scheme. In contrast to hybrid xc-functionals where the total energy values are Fourier interpolated, in the case of G_0W_0 , in the current implementation of `exciting`, only the self-energy correction term is interpolated and then added to a calculated DFT band-structure. The idea behind this approach is that the interpolation of the smaller correction terms causes smaller errors. The Wannier scheme, however, interpolates the full quasi-particle energies instead of the self-energy correction and calculates a consistent band-structure from them.

In the top panel of Fig. 4.4, both the Fourier and the Wannier band-structure is presented. The quasi-particle energies have been calculated on $4 \times 4 \times 1$ \mathbf{k} -points using the G_0W_0 approximation on top of a DFT calculation within the local density approximation (LDA). For this systems with a large unit cell such a coarse sampling corresponds to a 1D \mathbf{k} -point density of ~ 3.7 points per \AA^{-1} which suffices for a proper Wannier interpolation (compare Fig. 3.6). Additionally, in Fig. 4.4 the energy values being part of the support grid are displayed with yellow circles. These are the fixed points both interpolations have to pass. For the upper most valence bands there is not much difference between both interpolation schemes. In contrast, there are huge discrepancies in the conduction bands. In the bottom left panel, a region in the conduction bands around the zone center where huge differences emerge (blue shaded area) is magnified. We compare the magnified part of the band-structure with the corresponding area of the less dispersive DFT band-structure (bottom right panel) that has been calculated using LDA. The LDA band-structure shows three more dispersive parabolic bands bended upwards and two less dispersive bands from which one is bended downwards. The same features can be found in the Wannier interpolated quasi-particle band-structure while they are not visible in the Fourier interpolated one. This comparison gives rise to the claim that the Wannier interpolated quasi-particle band-structure is more likely physically correct than the Fourier interpolated one which shows unphysical strong oscillations and artificial band-crossings in the depicted region. In order to support this claim, we also provide the Wannier interpolated KS energies (black circles, bottom right panel). They almost

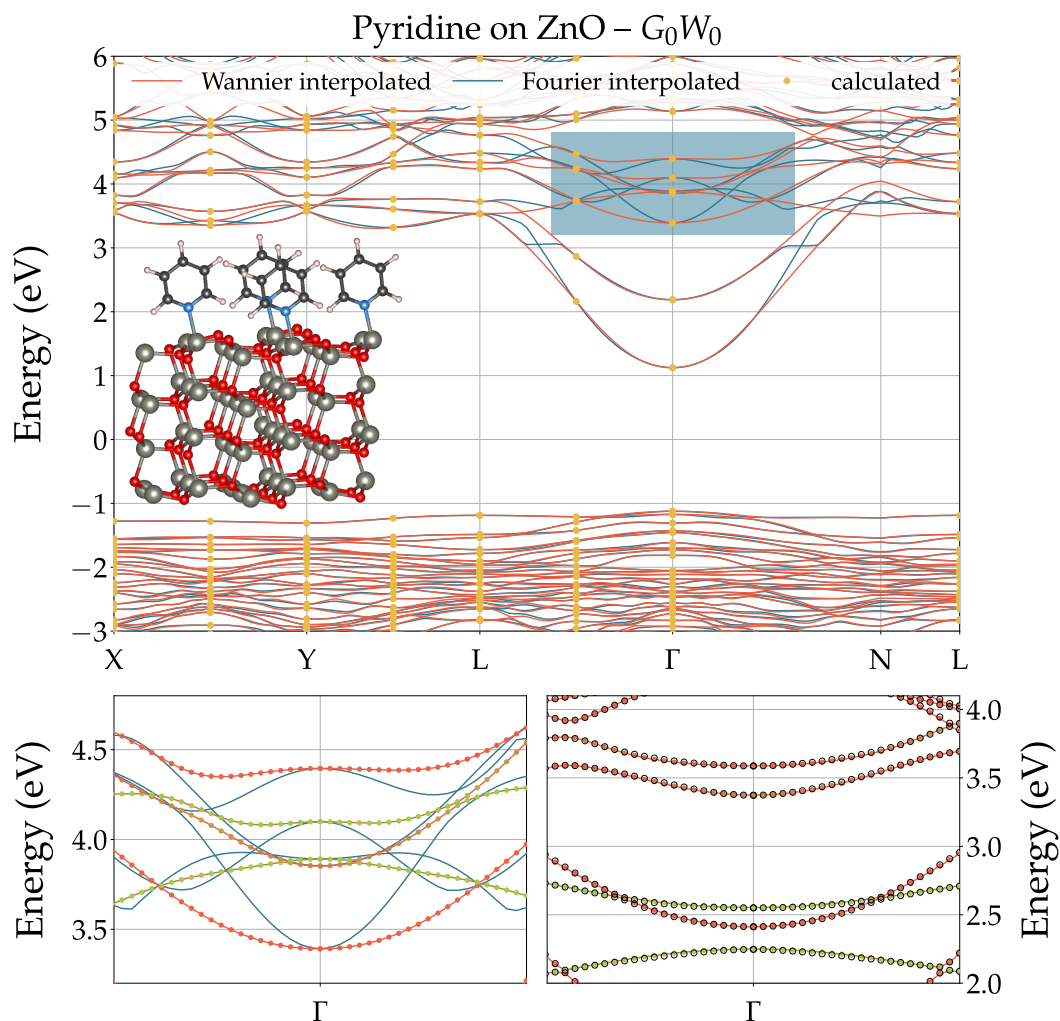


Fig. 4.4: Fourier and Wannier interpolated band-structure for pyridine on zinc oxide

The top panel shows the quasi-particle band-structure of a zinc oxide slab with pyridine molecules attached to the surface obtained using Fourier (blue) and Wannier (red) interpolation. The calculated points lying on the underlying \mathbf{k} -grid are given by yellow circles. The lower left panel magnifies the blue shaded region. The corresponding region of a DFT band-structure calculated within the LDA is illustrated in the lower right panel. Additionally, the band-character of the Wannier interpolated quasi-particle bands and the calculated KS bands in the lower panels is presented by red and green circles. The green bands originate from pyridine while the red bands predominantly stem from zinc oxide. The black circles in the lower right panel illustrate Wannier interpolated KS energies.

coincide with the calculated energies (colored dots) which supports the reliability of the Wannier interpolated quasi-particle band-structure. Furthermore, this shows that in this example the used BZ smapling suffices for a proper Wannier interpolation. Moreover, in

this particular example, Wannier interpolation shows that many-body perturbation theory within the G_0W_0 approximation does not only lead to an overall shift of the bands and an opening of the band-gap, but also rearranges the bands. This becomes more visible considering the character of the depicted bands (see Sec. 3.6.2). The red and green circles in the bottom panels indicate the character which was calculated using LDA (right panel) and which was Wannier interpolated from G_0W_0 quasi-particle energies (left panel), respectively. The LDA band-structure shows clearly two distinct bands that are attributed to pyridine (green) while the remaining three parabolic bands originate from the zinc oxide substrate (red). The same two pyridine bands can be found in the quasi-particle band-structure, but now being shifted upwards w.r.t. the ZnO bands. This means that the pyridine bands are shifted more than the bands of zinc oxide applying the self-energy correction, and the bands change their order compared to the LDA band-structure.

4.4. Metals

Here, we want to demonstrate that Wannier interpolation even works for metals. This seems to be a bit counter-intuitive since the method is based on the tight-binding approach which usually is not applicable to metals where the valence electrons are hardly bound to the nucleus. However, we find that eigenenergies in metals can be interpolated up to a high accuracy. We demonstrate this with the example of fcc silver. We have calculated the band-structure using KS-DFT with the PBE xc-functional on an $8 \times 8 \times 8$ \mathbf{k} -grid ($\cong 2.8 \mathbf{k}$ -points/ \AA^{-1}). In this case (and for most metals) it is not possible to select isolated subgroups of bands due to the lack of band-gaps (neglecting deep-lying semi-core states). Therefore, we generated WFs from 80 bands from which 65 are unoccupied at the Γ -point. As the lowest band, we choose one that is separated from the bands below by a finite energy gap. A comparison between the interpolated (red dashed lines) and the calculated band-structure (solid blue lines) shows that both the occupied and the low-lying unoccupied states are predicted with a high accuracy, i.e. there is no visible difference between both band-structures. However, the interpolation becomes more and more inaccurate the higher one goes in energy, and, for the bands close to the edge of the considered subspace (about 130 eV), there is a clear discrepancy between the calculated and the interpolated

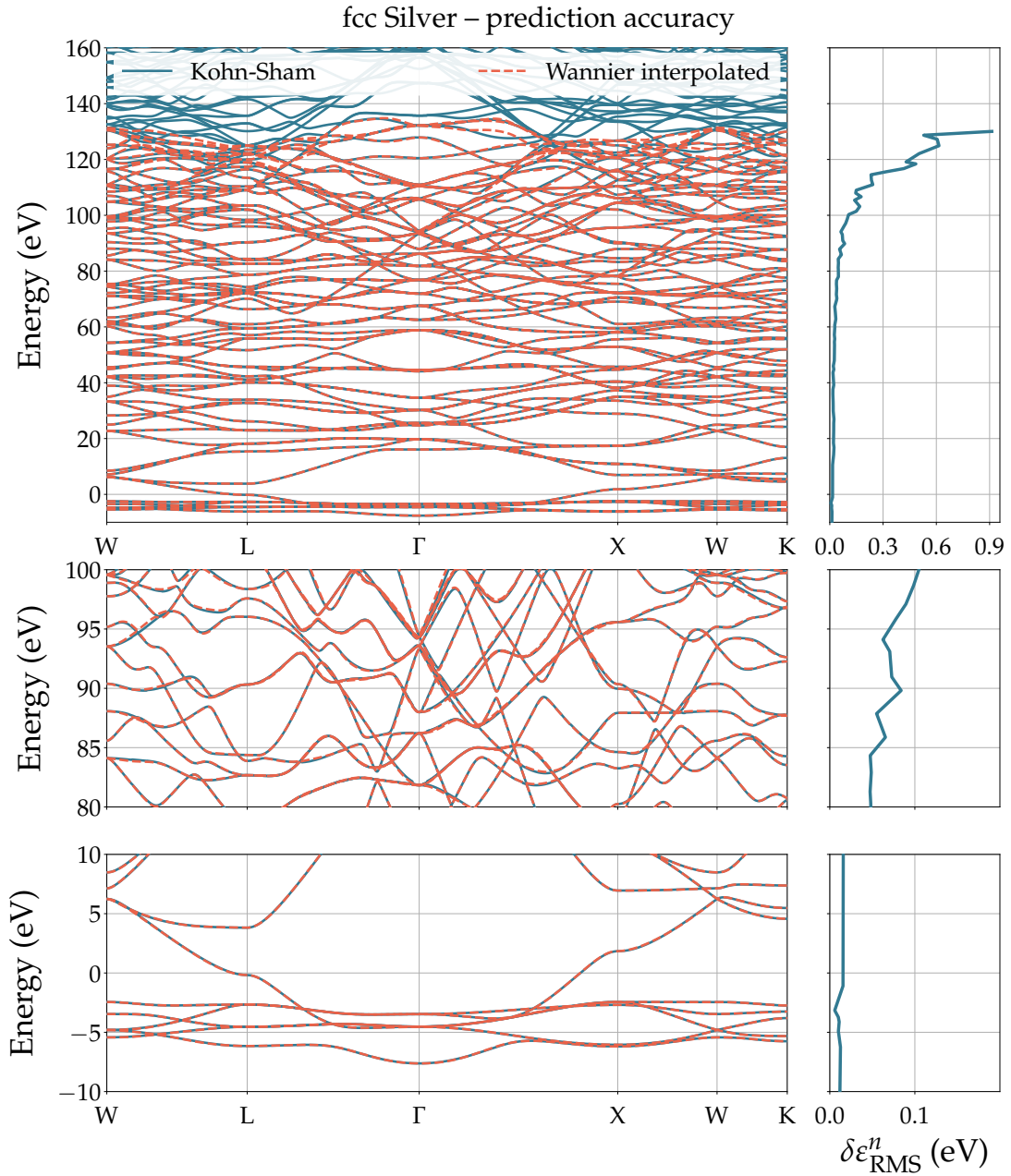


Fig. 4.5: Interpolated bandstructure of fcc silver

The prediction errors (right panels) remain below 100 meV up to an energy of 100 eV while being about one order of magnitude smaller for bands around the Fermi level (bottom panel).

bands. In order to quantify this qualitative observation we calculate the the RMS of the energy differences for each band separately

$$\delta\epsilon_{\text{RMS}}^n = \sqrt{\frac{1}{N} \sum_k (\epsilon_n^k - \tilde{\epsilon}_n^k)^2} \quad (4.2)$$

and plot it against the average band-energy $\sum_k \epsilon_n^k / N$ (right panels in Fig. 4.5).

We see that the prediction quality is quite high with an error below 20 meV around the Fermi level at zero (lower panel) and remains below 30 meV up to an energy of about 60 eV which corresponds to 37 bands (22 unoccupied). Even up to 90 eV or 55 (40) bands, the prediction error is smaller than 100 meV (mid-panel) before starting to increase for higher energies. In order to achieve a desired accurate interpolation for higher energies as well one has to take into account more unoccupied states in the generation of WFs. This will also improve the prediction for the lower bands since it corresponds to a larger tight-binding basis in which the states are expanded. The same behavior as shown here for silver, i.e. a drop in the interpolation quality for higher energies, can also be observed for different insulating and semi-conducting materials when considering such large subsets of several dozens or hundreds of entangled bands.

5. Conclusions and Outlook

We have implemented the generation of MLWFs within the (L)APW+lo method as implemented in the `exciting` code. It was found that the Wannier interpolation scheme using well and maximally localized WFs is capable to accurately and efficiently interpolate electronic eigenenergies over a wide energy range of 100 eV and more. TAs expected, the accuracy strongly depends on the density of the supporting \mathbf{k} -mesh. In the cases studied within this work densities of more than $3 \mathbf{k}\text{-points}/\text{\AA}^{-3}$ in one direction sufficed to interpolate energies within a few meV precision. Furthermore, when large ranges of dozens or hundreds of entangled bands are interpolated, the accuracy decreases with increasing energy, assumed that the lowest band selected was chosen to be separated from the bands below. However, the energy interval in which an interpolation is accurate and especially the accuracy for lower energy bands, become larger the bigger the number of bands is, from which WFs are constructed, is. We have also been able to successfully apply the Wannier interpolation scheme to metals and large and more complex systems with more than 40 atoms.

The tools presented here, allow for the calculation of proper band-structures based on more elaborate theoretical methods such as KS-DFT with non-local xc-functionals or many-body perturbation theory as implemented in the G_0W_0 approach. These methods do not provide direct access to energies and wavefunctions at arbitrary \mathbf{k} -points due to their high computational cost. In these cases, where interpolation schemes are indispensable, Wannier interpolation shows to be superior over the purely mathematical Fourier interpolation and is able to reproduce important physical features like degeneracies, band-crossings and splittings.

Concerning the construction of MLWFs, the use of OPFs turned out to be an extremely helpful tool to provide an initial guess for the subsequent localization algorithm. This is particularly crucial when considering large subgroups of entangled bands. In this case, it is almost impossible to have an idea of the corresponding MLWFs, especially if the nature and the origin of the bands is not known. Here, OPFs expanded in a large set of localized trial functions (local orbitals in this work) can provide a good starting point for a further minimization of the spread Ω . This enables the algorithm to get close to the global minimum of the spread functional. Yet, we did not always reach the global minimum in the case of entangled energy bands. This can be a consequence of an initial guess that was too far off from the global minimum, which, in turn, may be caused by the

strong localization of the local orbitals. We assume that trial functions that do not vanish in the interstitial region and that are not necessarily atom centered can provide a more suitable starting point using the OPF approach. Nevertheless, the spread Ω significantly decreases and the resulting WFs are well localized such that they are usable for accurate energy interpolations.

In addition to a steepest descent approach, we have further tested a CG algorithm with different update parameters in combination with a line-search algorithm. All the different CG algorithms perform much better than the steepest descent method. We speculate that a more efficient line-search or hybrid solutions with temporarily fixed step lengths could further improve the performance of the localization algorithm. However, this needs further investigations.

The ability to interpolate band-characters that are directly derived from the interpolated wavefunctions indicates that not just the eigenenergies but also the wavefunctions are interpolated correctly. That gives rise to the assumption that it should be possible to interpolate also numerous further quantities that are derived from the wavefunction. A possible example is the calculation of the exact position of the valence band maximum and the conduction band minimum and, accordingly, the band-gap as well as the calculation of the effective mass tensor. Further examples are matrix elements that occur in the calculation of optical properties which typically require dense BZ-samplings what limits the applicability of forefront methods due to the computational costs they come with. Another quantity that can be interpolated is the electron density within the self-consistent field cycle of a DFT calculation. This can be used to obtain a proper potential which may be useful for the calculation of metals which are normally hard to converge w.r.t. the number of \mathbf{k} -points.

References

- [AB99] Carlo Adamo and Vincenzo Barone. *Toward reliable density functional methods without adjustable parameters: The PBE0 model*. In: *The Journal of Chemical Physics* 110.13 (Mar. 1999), pp. 6158–6170. DOI: 10.1063/1.478522.
- [AG98] F Aryasetiawan and O Gunnarsson. *The GW method*. In: *Reports on Progress in Physics* 61.3 (Mar. 1998), pp. 237–312. DOI: 10.1088/0034-4885/61/3/002.
- [AQ07] Hazem Abu-Farsakh and Abdallah Qteish. *Ionicity scale based on the centers of maximally localized Wannier functions*. In: *Physical Review B* 75.8 (Feb. 2007), p. 085201. DOI: 10.1103/PhysRevB.75.085201.
- [Bjö96] Åke Björck. *Numerical Methods for Least Squares Problems*. Society for Industrial and Applied Mathematics, Jan. 1996. DOI: 10.1137/1.9781611971484.
- [Blo62] E. I. Blount. *Formalisms of Band Theory*. In: *Solid State Physics - Advances in Research and Applications*. Vol. 13. C. 1962, pp. 305–373. DOI: 10.1016/S0081-1947(08)60459-2.
- [Clo64] Jacques Des Cloizeaux. *Energy bands and projection operators in a crystal: Analytic and asymptotic properties*. In: *Physical Review* 135.3A (Aug. 1964), A685–A697. DOI: 10.1103/PhysRev.135.A685.
- [ER63] Clyde Edmiston and Klaus Ruedenberg. *Localized atomic and molecular orbitals*. In: *Reviews of Modern Physics* 35.3 (July 1963), pp. 457–464. DOI: 10.1103/RevModPhys.35.457.
- [FB60] J. M. Foster and S. F. Boys. *Canonical configurational interaction procedure*. In: *Reviews of Modern Physics* 32.2 (Apr. 1960), pp. 300–302. DOI: 10.1103/RevModPhys.32.300.
- [FR64] R. Fletcher and C. M. Reeves. *Function minimization by conjugate gradients*. In: *The Computer Journal* 7.2 (Feb. 1964), pp. 149–154. DOI: 10.1093/comjnl/7.2.149.

- [Gul+14] Andris Gulans and coworkers. *Exciting: a Full-Potential All-Electron Package Implementing Density-Functional Theory and Many-Body Perturbation Theory*. In: *Journal of Physics: Condensed Matter* 26.36 (2014), p. 363202. DOI: 10.1088/0953-8984/26/36/363202.
- [HF08] Gus L. W. Hart and Rodney W. Forcade. *Algorithm for generating derivative structures*. In: *Physical Review B* 77.22 (June 2008), p. 224115. DOI: 10.1103/PhysRevB.77.224115.
- [HK64] P. Hohenberg and W. Kohn. *Inhomogeneous Electron Gas*. In: *Physical Review* 136.3B (Nov. 1964), B864–B871. DOI: 10.1103/PhysRev.136.B864.
- [HS52] Magnus R. Hestenes and Eduard Stiefel. *Methods of Conjugate Gradients for Solving Linear Systems*. In: *Journal of Research of the National Bureau of Standards* 49.6 (1952), pp. 409–436.
- [Kan56] E O Kane. *Energy band structure in p-type germanium and silicon*. In: *J. Phys. Chem. Solids. Pergamon Press* 1 (1956), pp. 82–99.
- [KS65] W. Kohn and L. J. Sham. *Self-Consistent Equations Including Exchange and Correlation Effects*. In: *Physical Review* 140.4A (Nov. 1965), A1133–A1138. DOI: 10.1103/PhysRev.140.A1133.
- [LKW55] J M Luttinger, Kohn ', and W. *Motion of Electrons and Holes in Perturbed Periodic Fields*. In: *Physical Review* 97.4 (1955), pp. 869–883.
- [Löw50] Per-Olov Löwdin. *On the Non-Orthogonality Problem Connected with the Use of Atomic Wave Functions in the Theory of Molecules and Crystals*. In: *The Journal of Chemical Physics* 18.3 (Mar. 1950), pp. 365–375. DOI: 10.1063/1.1747632.
- [Mar+12] Nicola Marzari and coworkers. *Maximally localized Wannier functions: Theory and applications*. In: *Reviews of Modern Physics* 84.4 (2012), pp. 1419–1475. DOI: 10.1103/RevModPhys.84.1419.

- [MP76] Hendrik J. Monkhorst and James D. Pack. *Special points for Brillouin-zone integrations*. In: *Physical Review B* 13.12 (June 1976), pp. 5188–5192. DOI: 10.1103/PhysRevB.13.5188.
- [Mus+15] Jamal I. Mustafa and coworkers. *Automated construction of maximally localized Wannier functions: Optimized projection functions method*. In: *Physical Review B* 92.16 (Oct. 2015), p. 165134. DOI: 10.1103/PhysRevB.92.165134.
- [MV97] Nicola Marzari and David Vanderbilt. *Maximally-localized generalized Wannier functions for composite energy bands*. In: *Physical Review B* 56.20 (1997), pp. 12847–12865. DOI: 10.1103/PhysRevB.56.12847.
- [Nie72] W. von Niessen. *Density Localization of Atomic and Molecular Orbitals. I*. In: *The Journal of Chemical Physics* 56.9 (May 1972), pp. 4290–4297. DOI: 10.1063/1.1677859.
- [PA07] Clas Persson and Claudia Ambrosch-Draxl. *A full-band FPLAPW + k . p method for solving the Kohn-Sham equation*. In: *Computer Physics Communications* 177.3 (2007), pp. 280–287. DOI: 10.1016/j.cpc.2007.02.111.
- [PBE96] John P. Perdew, Kieron Burke, and Matthias Ernzerhof. *Generalized Gradient Approximation Made Simple*. In: *Physical Review Letters* 77.18 (Oct. 1996), pp. 3865–3868. DOI: 10.1103/PhysRevLett.77.3865.
- [PKA88] Warren E. Pickett, Henry Krakauer, and Philip B. Allen. *Smooth Fourier interpolation of periodic functions*. In: *Physical Review B* 38.4 (1988), pp. 2721–2726. DOI: 10.1103/PhysRevB.38.2721.
- [PL09] David Prendergast and Steven G. Louie. *Bloch-state-based interpolation: An efficient generalization of the Shirley approach to interpolating electronic structure*. In: *Physical Review B - Condensed Matter and Materials Physics* 80.23 (2009), pp. 1–10. DOI: 10.1103/PhysRevB.80.235126.
- [PM89] János Pipek and Paul G. Mezey. *A fast intrinsic localization procedure applicable for ab initio and semiempirical linear combination of atomic orbital wave*

- functions*. In: *The Journal of Chemical Physics* 90.9 (May 1989), pp. 4916–4926. DOI: 10.1063/1.456588.
- [PR69] E Polak and G Ribiere. *Note sur la convergence de méthodes de directions conjuguées*. In: *Revue française d’informatique et de recherche opérationnelle* 3 (1969), pp. 35–43.
- [Shi96] EL Shirley. *Optimal basis sets for detailed Brillouin-zone intergrations*. In: *Physical Review B* 54.23 (1996), pp. 464–469. DOI: 10.1103/PhysRevB.54.16464.
- [SK54] J. C. Slater and G. F. Koster. *Simplified LCAO Method for the Periodic Potential Problem*. In: *Physical Review* 94.6 (June 1954), pp. 1498–1524. DOI: 10.1103/PhysRev.94.1498.
- [Wan37] Gregory H. Wannier. *The structure of electronic excitation levels in insulating crystals*. In: *Physical Review* 52.3 (1937), pp. 191–197. DOI: 10.1103/PhysRev.52.191.
- [Yat+07] Jonathan R. Yates and coworkers. *Spectral and Fermi surface properties from Wannier interpolation*. In: *Physical Review B* 75.19 (May 2007), p. 195121. DOI: 10.1103/PhysRevB.75.195121.

List of Figures

3.1. Flowchart of the Wannierization procedure	26
3.2. WFs in SiC from simple projection on carbon and silicon s - and p -orbitals	29
3.3. Local minimum for SiC reached from simple projection	36
3.4. Global minimum for SiC reached from OPF	37
3.5. Convergence of different minimization methods	38
3.6. \mathbf{k} -point convergence of the prediction error and the spread Ω	40
3.7. Real-space lattice vectors on Wigner-Seitz super cell	41
4.1. Fourier and Wannier interpolated band-structure for diamond	46
4.2. MLWFs in group IV and III-V semiconductors	49
4.3. Interpolated band-structure of TiO_2 indicating the atomic character . . .	51
4.4. Fourier and Wannier interpolated band-structure for pyridine on zinc oxide	53
4.5. Interpolated bandstructure of fcc silver	55

List of Abbreviations and Symbols

APW augmented plane wave

BZ first Brillouin zone

CG conjugate gradient

DFT density-functional theory

I interstitial region

KS Kohn–Sham

MLWF maximally localized Wannier function

MT muffin-tin sphere

OPF optimized projection function

SC supercell

WF Wannier function

Frequently used Symbols

$\Psi_{n,\mathbf{k}}, n\mathbf{k}\rangle$	Bloch wavefunction
$\psi_{n,\mathbf{k}}$	gauche transformed (mixed) Bloch wavefunction
$w_{n,\mathbf{R}}, n\mathbf{R}\rangle$	Wannier function
\mathbf{k}	wavevector on the original (coarse) \mathbf{k} -grid
\mathbf{q}	wavevector on the interpolation (fine) \mathbf{k} -grid
\mathbf{b}	vector connecting a \mathbf{k} -point with one of its nearest neighbors
$w_{\mathbf{b}}$	corresponding geometric weight of \mathbf{b}
$w = \sum_{\mathbf{b}} w_{\mathbf{b}}$	sum of geometric weights
\mathbf{R}	real-space lattice vector
\mathbf{G}	reciprocal-space lattice vector

$U^{\mathbf{k}}$	(semi)unitary transformation from Hamiltonian gauge to Wannier gauge
$V^{\mathbf{q}}$	unitary transformation from Wannier gauge to Hamiltonian gauge
$\mathcal{M}^{\mathbf{k},\mathbf{b}}$	plane wave matrix elements in original Bloch states
$M^{\mathbf{k},\mathbf{b}}$	plane wave matrix elements in transformed Bloch states
Ω	spread functional
$\langle \mathbf{r} \rangle_n$	center of a Wannier function
J	number of bands under consideration

Selbstständigkeitserklärung

Ich erkläre hiermit, dass ich die vorliegende Arbeit selbstständig verfasst und noch nicht für andere Prüfungen eingereicht habe. Sämtliche Quellen einschließlich Internetquellen, die unverändert oder abgewandelt wiedergegeben werden, insbesondere Quellen für Texte, Grafiken, Tabellen und Bilder, sind als solche kenntlich gemacht. Mir ist bekannt, dass bei Verstößen gegen diese Grundsätze ein Verfahren wegen Täuschungsversuchs bzw. Täuschung eingeleitet wird.

Berlin, den 12.01.2018

Appendix A Implementation of plane wave matrix elements

In the (L)APW+lo basis, the plane wave matrix elements can be split up into two contributions from the muffin-tin region and the interstitial region, respectively

$$\langle \mu \mathbf{k} | e^{-i\mathbf{b}\cdot\mathbf{r}} | \nu \mathbf{k} + \mathbf{b} \rangle^\Omega = \langle \mu \mathbf{k} | e^{-i\mathbf{b}\cdot\mathbf{r}} | \nu \mathbf{k} + \mathbf{b} \rangle^{\text{MT}} + \langle \mu \mathbf{k} | e^{-i\mathbf{b}\cdot\mathbf{r}} | \nu \mathbf{k} + \mathbf{b} \rangle^{\text{IR}}, \quad (\text{A.1})$$

with

$$\langle \mu \mathbf{k} | e^{-i\mathbf{b}\cdot\mathbf{r}} | \nu \mathbf{k} + \mathbf{b} \rangle^{\text{MT}} = \sum_{\alpha} \int_{\text{MT}_{\alpha}} d\mathbf{r} \overline{\Psi_{\mu,\mathbf{k}}^{\alpha}}(\mathbf{r}) e^{-i\mathbf{b}\cdot\mathbf{r}} \Psi_{\nu,\mathbf{k}+\mathbf{b}}^{\alpha}(\mathbf{r}), \quad (\text{A.2})$$

where sum runs over all atomic sites α and

$$\langle \mu \mathbf{k} | e^{-i\mathbf{b}\cdot\mathbf{r}} | \nu \mathbf{k} + \mathbf{b} \rangle^{\text{IR}} = \int_{\text{IR}} d\mathbf{r} \overline{\Psi_{\mu,\mathbf{k}}^{\text{IR}}}(\mathbf{r}) e^{-i\mathbf{b}\cdot\mathbf{r}} \Psi_{\nu,\mathbf{k}+\mathbf{b}}^{\text{IR}}(\mathbf{r}). \quad (\text{A.3})$$

In one specific MT α , the wavefunction takes the following form

$$\begin{aligned} \Psi_{\mu,\mathbf{k}}^{\alpha}(\mathbf{r}) &= \sum_{\mathbf{G}} C_{\mu,\mathbf{G}}^{\mathbf{k}} \sum_{l,m} \sum_{o=1}^{M_l^{\alpha}} A_{lm,o,\mathbf{G}+\mathbf{k}}^{\alpha} u_{l,o}^{\alpha}(r_{\alpha}) Y_{lm}(\hat{\mathbf{r}}_{\alpha}) \\ &+ \sum_{\mathbf{L}} C_{\mu,\mathbf{L}}^{\mathbf{k}} f_{l_L}^{\mathbf{L}}(r_{\alpha_L}) Y_{l_L m_L}(\hat{\mathbf{r}}_{\alpha_L}) \delta_{\alpha\alpha_L}, \end{aligned} \quad (\text{A.4})$$

where $\mathbf{r}_{\alpha} = \mathbf{r} - \mathbf{R}_{\alpha}$, and the second sum runs over all local orbitals that are characterized by the combined index $\mathbf{L} = (\mathbf{R}_{\alpha_L}, R_{\text{MT}_{\alpha_L}}, l_L, m_L)$. Further, we express the plane waves in terms of spherical harmonics and spherical Bessel functions of first kind using the Rayleigh expansion

$$\begin{aligned} e^{-i\mathbf{b}\cdot\mathbf{r}} &= e^{-i\mathbf{b}\cdot\mathbf{R}_{\alpha}} e^{-i\mathbf{b}\cdot\mathbf{r}_{\alpha}} \\ &= 4\pi e^{-i\mathbf{b}\cdot\mathbf{R}_{\alpha}} \sum_{l,m} (-i)^l j_l(br_{\alpha}) \overline{Y_{lm}(\hat{\mathbf{b}})} Y_{lm}(\hat{\mathbf{r}}_{\alpha}). \end{aligned} \quad (\text{A.5})$$

With that the total MT contribution of the plane wave matrix elements splits up into four distinct parts

$$\begin{aligned}
 \langle \mu \mathbf{k} | e^{-i\mathbf{b}\cdot\mathbf{r}} | \nu \mathbf{k} + \mathbf{b} \rangle^{\text{MT}} &= 4\pi \sum_{\mathbf{G}, \mathbf{G}'} \overline{C_{\mu, \mathbf{G}}^{\mathbf{k}}} C_{\nu, \mathbf{G}'}^{\mathbf{k}+\mathbf{b}} \mathcal{A} \mathcal{A}_{\mathbf{G}, \mathbf{G}'}^{\mathbf{k}, \mathbf{b}} \\
 &+ 4\pi \sum_{\mathbf{G}, \mathbf{L}} \overline{C_{\mu, \mathbf{G}}^{\mathbf{k}}} C_{\nu, \mathbf{L}}^{\mathbf{k}+\mathbf{b}} \mathcal{A} \mathcal{L}_{\mathbf{G}, \mathbf{L}}^{\mathbf{k}, \mathbf{b}} \\
 &+ 4\pi \sum_{\mathbf{G}', \mathbf{L}} \overline{C_{\mu, \mathbf{L}}^{\mathbf{k}}} C_{\nu, \mathbf{G}'}^{\mathbf{k}+\mathbf{b}} \mathcal{L} \mathcal{A}_{\mathbf{L}, \mathbf{G}'}^{\mathbf{k}, \mathbf{b}} \\
 &+ 4\pi \sum_{\mathbf{L}, \mathbf{L}'} \overline{C_{\mu, \mathbf{L}}^{\mathbf{k}}} C_{\nu, \mathbf{L}'}^{\mathbf{k}+\mathbf{b}} \mathcal{L} \mathcal{L}_{\mathbf{L}, \mathbf{L}'}^{\mathbf{k}, \mathbf{b}} \quad ,
 \end{aligned} \tag{A.6}$$

where the indices \mathbf{G} and \mathbf{G}' label the $\mathbf{G} + \mathbf{k}$ vectors corresponding to the wavefunctions at \mathbf{k} -point \mathbf{k} and $\mathbf{k} + \mathbf{b}$, respectively and \mathbf{L} and \mathbf{L}' label the local orbitals. The four parts correspond to an APW–APW term ($\mathcal{A}\mathcal{A}$), an lo–lo term ($\mathcal{L}\mathcal{L}$) and two mixed terms ($\mathcal{A}\mathcal{L}$ and $\mathcal{L}\mathcal{A}$) which are given by the expressions

$$\begin{aligned}
 \mathcal{A} \mathcal{A}_{\mathbf{G}, \mathbf{G}'}^{\mathbf{k}, \mathbf{b}} &= \sum_{\alpha} e^{-i\mathbf{b}\cdot\mathbf{R}_{\alpha}} \sum_{l, m, o} \sum_{l', m', o'} \overline{A_{lm, o, \mathbf{G}+\mathbf{k}}^{\alpha}} A_{l'm', o', \mathbf{G}'+\mathbf{k}+\mathbf{b}}^{\alpha} \\
 &\times \sum_{l'', m''} (-i)^{l''} \overline{Y_{l'' m''}(\hat{\mathbf{b}})} \mathcal{G}_{lm, l' m'}^{l'' m''} \int_0^{R_{\text{MT}\alpha}} u_{l, o}^{\alpha}(r) j_{l''}(br) u_{l', o'}^{\alpha}(r) r^2 dr \quad ,
 \end{aligned} \tag{A.7}$$

$$\begin{aligned}
 \mathcal{A} \mathcal{L}_{\mathbf{G}, \mathbf{L}'}^{\mathbf{k}, \mathbf{b}} &= \sum_{\alpha} e^{-i\mathbf{b}\cdot\mathbf{R}_{\alpha}} \delta_{\alpha\alpha_{\mathbf{L}'}} \sum_{l, m, o} \overline{A_{lm, o, \mathbf{G}+\mathbf{k}}^{\alpha}} \\
 &\times \sum_{l'', m''} (-i)^{l''} \overline{Y_{l'' m''}(\hat{\mathbf{b}})} \mathcal{G}_{lm, l' m'}^{l'' m''} \int_0^{R_{\text{MT}\alpha}} u_{l, o}^{\alpha}(r) j_{l''}(br) f_{l', \mathbf{L}'}^{l''}(r) r^2 dr \quad ,
 \end{aligned} \tag{A.8}$$

$$\begin{aligned}
 \mathcal{L} \mathcal{A}_{\mathbf{L}, \mathbf{G}'}^{\mathbf{k}, \mathbf{b}} &= \sum_{\alpha} e^{-i\mathbf{b}\cdot\mathbf{R}_{\alpha}} \delta_{\alpha\alpha_{\mathbf{L}}} \sum_{l, m, o} A_{lm, o, \mathbf{G}'+\mathbf{k}+\mathbf{b}}^{\alpha} \\
 &\times \sum_{l'', m''} (-i)^{l''} \overline{Y_{l'' m''}(\hat{\mathbf{b}})} \mathcal{G}_{l_L m_L, lm}^{l'' m''} \int_0^{R_{\text{MT}\alpha}} u_{l, o}^{\alpha}(r) j_{l''}(br) f_{l_L}^{l''}(r) r^2 dr
 \end{aligned} \tag{A.9}$$

and

$$\begin{aligned} \mathcal{L}\mathcal{L}_{L,L'}^{\mathbf{k},\mathbf{b}} &= \sum_{\alpha} e^{-i\mathbf{b}\cdot\mathbf{R}_{\alpha}} \delta_{\alpha\alpha_L} \delta_{\alpha\alpha_{L'}} \\ &\times \sum_{l'',m''} (-i)^{l''} \overline{Y_{l''m''}}(\hat{\mathbf{b}}) \mathcal{G}_{l_L m_L, l_{L'} m_{L'}}^{l'' m''} \int_0^{R_{\text{MT}\alpha}} f_{l_L}^L(r) j_{l''}(br) f_{l_{L'}}^{L'}(r) r^2 dr \quad . \end{aligned} \quad (\text{A.10})$$

Here, $\mathcal{G}_{l m, l' m'}^{l'' m''}$ denotes the Gaunt coefficients $\langle Y_{lm} | Y_{l'' m''} | Y_{l' m'} \rangle$. Introducing the new combined index $\lambda = (l, m, o)$, we can express the total MT contribution with the following matrix-matrix multiplications, where $\{X_{i,j}\}$ indicates (sub)matrices and i and j serve as a reminder to the dimension and indexing of the matrix X

$$\langle \mathbf{k} | e^{-i\mathbf{b}\cdot\mathbf{r}} | \mathbf{k} + \mathbf{b} \rangle^{\text{MT}} = 4\pi \left[\begin{array}{c} \{C_{\mathbf{G},\mu}^{\mathbf{k}}\} \\ \{C_{L,\mu}^{\mathbf{k}}\} \end{array} \right]^{\dagger} \left[\begin{array}{c|c} \{\mathcal{A}\mathcal{A}_{\mathbf{G},\mathbf{G}'}^{\mathbf{k},\mathbf{b}}\} & \{\mathcal{A}\mathcal{L}_{\mathbf{G},L'}^{\mathbf{k},\mathbf{b}}\} \\ \hline \{\mathcal{L}\mathcal{A}_{L,\mathbf{G}'}^{\mathbf{k},\mathbf{b}}\} & \{\mathcal{L}\mathcal{L}_{L,L'}^{\mathbf{k},\mathbf{b}}\} \end{array} \right] \left[\begin{array}{c} \{C_{\mathbf{G}',\nu}^{\mathbf{k}+\mathbf{b}}\} \\ \{C_{L,\nu}^{\mathbf{k}+\mathbf{b}}\} \end{array} \right] \quad (\text{A.11})$$

and

$$\begin{aligned} \{\mathcal{A}\mathcal{A}_{\mathbf{G},\mathbf{G}'}^{\mathbf{k},\mathbf{b}}\} &= \sum_{\alpha} \{A_{\lambda,\mathbf{G}+\mathbf{k}}^{\alpha}\}^{\dagger} \{J_{\lambda,\lambda'}^{\alpha,\mathbf{b}}\} \{A_{\lambda,\mathbf{G}'+\mathbf{k}+\mathbf{b}}^{\alpha}\} \quad , \\ \{\mathcal{A}\mathcal{L}_{\mathbf{G},L'}^{\mathbf{k},\mathbf{b}}\} &= \sum_{\alpha} \{A_{\lambda,\mathbf{G}+\mathbf{k}}^{\alpha}\}^{\dagger} \{J_{\lambda,L'}^{\alpha,\mathbf{b}}\} \quad , \\ \{\mathcal{L}\mathcal{A}_{L,\mathbf{G}'}^{\mathbf{k},\mathbf{b}}\} &= \sum_{\alpha} \{J_{L,\lambda}^{\alpha,\mathbf{b}}\} \{A_{\lambda,\mathbf{G}'+\mathbf{k}+\mathbf{b}}^{\alpha}\} \quad , \\ \{\mathcal{L}\mathcal{L}_{L,L'}^{\mathbf{k},\mathbf{b}}\} &= \sum_{\alpha} \{J_{L,L'}^{\alpha,\mathbf{b}}\} \quad . \end{aligned} \quad (\text{A.12})$$

The matrices $J^{\alpha, \mathbf{b}}$ contain the sums over the radial integrals times the Gaunt coefficients

$$\begin{aligned}
 J_{\lambda, \lambda'}^{\alpha, \mathbf{b}} &= e^{-i\mathbf{b} \cdot \mathbf{R}_\alpha} \sum_{l'', m''} (-i)^{l''} \overline{Y_{l'' m''}}(\hat{\mathbf{b}}) \mathcal{G}_{l_\lambda m_\lambda, l_{\lambda'} m_{\lambda'}}^{l'' m''} \int_0^{R_{\text{MT}\alpha}} u_\lambda^\alpha(r) j_{l''}(br) u_{\lambda'}^\alpha(r) r^2 dr \quad , \\
 J_{\lambda, L'}^{\alpha, \mathbf{b}} &= e^{-i\mathbf{b} \cdot \mathbf{R}_\alpha} \delta_{\alpha\alpha_{L'}} \sum_{l'', m''} (-i)^{l''} \overline{Y_{l'' m''}}(\hat{\mathbf{b}}) \mathcal{G}_{l_\lambda m_\lambda, l_{L'} m_{L'}}^{l'' m''} \int_0^{R_{\text{MT}\alpha}} u_\lambda^\alpha(r) j_{l''}(br) f_{L'}^{L'}(r) r^2 dr \quad , \\
 J_{L, \lambda}^{\alpha, \mathbf{b}} &= e^{-i\mathbf{b} \cdot \mathbf{R}_\alpha} \delta_{\alpha\alpha_L} \sum_{l'', m''} (-i)^{l''} \overline{Y_{l'' m''}}(\hat{\mathbf{b}}) \mathcal{G}_{l_L m_L, l_\lambda m_\lambda}^{l'' m''} \int_0^{R_{\text{MT}\alpha}} u_\lambda^\alpha(r) j_{l''}(br) f_L^L(r) r^2 dr \quad , \\
 J_{L, L'}^{\alpha, \mathbf{b}} &= e^{-i\mathbf{b} \cdot \mathbf{R}_\alpha} \delta_{\alpha\alpha_L} \delta_{\alpha\alpha_{L'}} \sum_{l'', m''} (-i)^{l''} \overline{Y_{l'' m''}}(\hat{\mathbf{b}}) \mathcal{G}_{l_L m_L, l_{L'} m_{L'}}^{l'' m''} \int_0^{R_{\text{MT}\alpha}} f_L^L(r) j_{l''}(br) f_{L'}^{L'}(r) r^2 dr \quad .
 \end{aligned} \tag{A.13}$$

Notice that the latter matrices are independent of the \mathbf{k} -point and band-indices under consideration and thus just need to be calculated once for all required vectors \mathbf{b} . All the dependence on the band-indices μ and ν is contained in the multiplication with the eigenvector matrices C in (A.11) which is inexpensive and the final step in the implementation. So, besides the calculation of the $J^{\alpha, \mathbf{b}}$ and the matching coefficients A^α , everything is broken down to simple matrix-matrix multiplications which can be performed well in parallel.

In the interstitial region, the wavefunction is given by a simple plane wave expansion

$$\Psi_{\mu, \mathbf{k}}^{\text{IR}}(\mathbf{r}) = \frac{1}{\sqrt{\Omega}} \sum_{\mathbf{G}} C_{\mu, \mathbf{G}}^{\mathbf{k}} e^{i(\mathbf{G} + \mathbf{k}) \cdot \mathbf{r}} \quad . \tag{A.14}$$

We now consider the more general matrix elements

$$\begin{aligned}
 \langle \mu \mathbf{k} | e^{-i(\mathbf{b} + \tilde{\mathbf{G}}) \cdot \mathbf{r}} | \nu \mathbf{k} + \mathbf{b} \rangle^{\text{IR}} &= \int_{\text{IR}} d\mathbf{r} \overline{\Psi_{\mu, \mathbf{k}}^{\text{IR}}(\mathbf{r})} e^{-i(\mathbf{b} + \tilde{\mathbf{G}}) \cdot \mathbf{r}} \Psi_{\nu, \mathbf{k} + \mathbf{b}}^{\text{IR}}(\mathbf{r}) \\
 &= \frac{1}{\Omega} \sum_{\mathbf{G}, \mathbf{G}'} \int_{\Omega} d\mathbf{r} \theta_{\text{IR}}(\mathbf{r}) \overline{C_{\mu, \mathbf{G}}^{\mathbf{k}}} e^{-i(\mathbf{G} + \mathbf{k}) \cdot \mathbf{r}} e^{-i(\mathbf{b} + \tilde{\mathbf{G}}) \cdot \mathbf{r}} C_{\nu, \mathbf{G}'}^{\mathbf{k} + \mathbf{b}} e^{i(\mathbf{G}' + \mathbf{k} + \mathbf{b}) \cdot \mathbf{r}} \\
 &= \frac{1}{\Omega} \int_{\Omega} d\mathbf{r} \theta_{\text{IR}}(\mathbf{r}) \sum_{\mathbf{G}} \overline{C_{\mu, \mathbf{G}}^{\mathbf{k}}} e^{i\mathbf{G} \cdot \mathbf{r}} \sum_{\mathbf{G}'} C_{\nu, \mathbf{G}'}^{\mathbf{k} + \mathbf{b}} e^{i\mathbf{G}' \cdot \mathbf{r}} e^{-i\tilde{\mathbf{G}} \cdot \mathbf{r}} \quad ,
 \end{aligned} \tag{A.15}$$

where $\theta_{\text{IR}}(\mathbf{r})$ is the interstitial region characteristic function which is 0 inside the muffintins and 1 otherwise. Using the Fourier transform $\mathcal{F}[f]$ and its inverse, Eq. (A.15) can be rewritten as

$$\langle \mu_{\mathbf{k}} | e^{-i(\mathbf{b} + \tilde{\mathbf{G}}) \cdot \mathbf{r}} | \nu_{\mathbf{k} + \mathbf{b}} \rangle^{\text{IR}} = \mathcal{F} \left[\theta_{\text{IR}}(\mathbf{r}) \overline{\mathcal{F}^{-1} [C_{\mu, \mathbf{G}}^{\mathbf{k}}] (\mathbf{r})} \mathcal{F}^{-1} [C_{\nu, \mathbf{G}'}^{\mathbf{k} + \mathbf{b}}] (\mathbf{r}) \right] (\tilde{\mathbf{G}}). \quad (\text{A.16})$$

Evaluating this Fourier transform at $\tilde{\mathbf{G}} = 0$ yields the desired interstitial contribution of the plane wave matrix elements. In practice, the characteristic function in real space is also obtained from the inverse Fourier transform of the characteristic function in reciprocal space $\theta_{\text{IR}}(\mathbf{r}) = \mathcal{F}^{-1}[\hat{\theta}_{\text{IR}}(\mathbf{G})](\mathbf{r})$.